
EVIDENTIAL DEEP LEARNING WITH SPECTRAL-SPATIAL UNCERTAINTY DISENTANGLEMENT FOR OPEN-SET HYPERSPPECTRAL DOMAIN GENERALIZATION

Amirreza Khoshbakht

Faculty of Engineering and Natural Sciences (VPALab),
Sabanci University, Türkiye
amirreza.khoshbakht@sabanciuniv.edu

Erchan Aptoula

Faculty of Engineering and Natural Sciences (VPALab),
Sabanci University, Türkiye
erchan.aptoula@sabanciuniv.edu

ABSTRACT

Open-set domain generalization(OSDG) for hyperspectral image classification presents significant challenges due to the presence of unknown classes in target domains and the need for models to generalize across multiple unseen domains without target-specific adaptation. Existing domain adaptation methods assume access to target domain data during training and fail to address the fundamental issue of domain shift when unknown classes are present, leading to negative transfer and reduced classification performance. To address these limitations, we propose a novel open-set domain generalization framework that combines four key components: Spectrum-Invariant Frequency Disentanglement (SIFD) for domain-agnostic feature extraction, Dual-Channel Residual Network (DCRN) for robust spectral-spatial feature learning, Evidential Deep Learning (EDL) for uncertainty quantification, and Spectral-Spatial Uncertainty Disentanglement (SSUD) for reliable open-set classification. The SIFD module extracts domain-invariant spectral features in the frequency domain through attention-weighted frequency analysis and domain-agnostic regularization, while DCRN captures complementary spectral and spatial information via parallel pathways with adaptive fusion. EDL provides principled uncertainty estimation using Dirichlet distributions, enabling the SSUD module to make reliable open-set decisions through uncertainty-aware pathway weighting and adaptive rejection thresholding. Experimental results on three cross-scene hyperspectral classification tasks show that our approach achieves performance comparable to state-of-the-art domain adaptation methods while requiring no access to the target domain during training. The implementation will be made available at <https://github.com/amir-khb/SSUDOSDG> upon acceptance.

Keywords Open-set recognition · Domain generalization · Hyperspectral image classification · Uncertainty quantification

1 Introduction

Hyperspectral image (HSI) classification has emerged as a fundamental task in remote sensing applications, providing critical insights for precision agriculture, environmental monitoring, geological exploration, and urban planning [1–6]. The rich spectral-spatial information contained in hyperspectral data, spanning hundreds of narrow contiguous wavelength bands, enables the identification and classification of diverse land cover materials based on their unique spectral signatures. However, the practical deployment of HSI classification models faces significant challenges when applied across different geographical locations, temporal periods, or sensor configurations, where domain shifts occur due to varying atmospheric conditions, illumination changes, and sensor characteristics [7–11].

Traditional domain adaptation (DA) approaches have been widely applied to address cross-domain HSI classification challenges by leveraging labeled source domain data alongside limited target domain samples during training [8, 12, 13]. These methods typically assume that the source and target domains share the same label space and that labeled target samples are available for model adaptation. However, such assumptions are often violated in real-world scenarios, where target domains may contain unknown classes not present in the source domain, and obtaining labeled target data is expensive, time-consuming, or simply infeasible due to operational constraints [14, 15]. The failure to account for unknown classes can lead to negative transfer phenomena, where the model incorrectly maps unknown target samples to known source classes, significantly degrading classification performance and reliability [16, 17].

Open-set domain adaptation (OSDA) has emerged as a promising solution to address the presence of unknown classes in target domains while performing cross-domain transfer [17, 18]. Recent OSDA methods for HSI classification, such as WGDG [19], employ weighted generative adversarial networks and dynamic thresholding to identify and reject unknown classes while adapting to known class distributions. However, these approaches still require access to unlabeled target domain data during training, limiting their applicability in scenarios where target domains are entirely unavailable during model development.

Domain generalization (DG) represents a more challenging yet practical paradigm that aims to learn domain-invariant representations from source domains alone, enabling direct application to unseen target domains without any target data access during training [20, 21]. While recent DG methods for HSI classification have shown promising results through techniques such as disentangled representation learning [20] and dual-attention mechanisms [21], they primarily address closed-set scenarios where all target classes are assumed to be present in the source domain. The combination of open-set recognition with domain generalization—termed open-set domain generalization (OSDG)—remains largely unexplored in the hyperspectral imaging domain, despite its critical importance for real-world deployment scenarios [22, 23].

In this article, we propose a novel open-set domain generalization framework specifically designed for cross-scene HSI classification that operates without requiring any target domain data during training while effectively handling unknown classes during inference. Our approach integrates four key components: Spectrum-Invariant Frequency Disentanglement (SIFD) for extracting domain-agnostic spectral features, Dual-Channel Residual Network (DCRN) for robust spectral-spatial feature learning, Evidential Deep Learning (EDL) for principled uncertainty quantification, and Spectral-Spatial Uncertainty Disentanglement (SSUD) for reliable open-set classification. The SIFD module operates in the frequency domain to identify and extract domain-invariant spectral components while suppressing domain-specific variations through attention-weighted feature selection and domain-agnostic regularization. The DCRN architecture captures complementary spectral and spatial information through parallel processing pathways that are subsequently fused using adaptive attention mechanisms, ensuring comprehensive feature representation for both known and unknown class detection.

The main contributions of this work can be summarized as follows: 1) We introduce the first comprehensive open-set domain generalization framework for HSI classification that effectively handles unknown classes without requiring target domain data during training. 2) We use a spectrum-invariant frequency disentanglement module that extracts domain-agnostic features in the frequency domain through attention-weighted analysis and domain-neutral regularization. 3) We develop a dual-channel residual network architecture with evidential deep learning for robust spectral-spatial feature extraction and uncertainty quantification across multiple domains. 4) We design a spectral-spatial uncertainty disentanglement mechanism that adaptively weights pathway-specific uncertainties for reliable open-set classification decisions. The experimental results on three cross-scene HSI classification tasks demonstrate that our approach achieves comparable performance with state-of-the-art domain adaptation methods while requiring no target domain access during training, establishing a new paradigm for practical open-set domain generalization in hyperspectral imaging.

The remainder of this article is organized as follows: Section 2 reviews related work on domain adaptation, domain generalization, and open-set recognition for HSI classification. Section 3 presents the detailed methodology of our proposed framework. Section 4 provides comprehensive experimental results and analysis. Section 5 concludes the article with future research directions.

2 Related Works

2.1 Unsupervised Domain Adaptation for HSI Classification

Unsupervised domain adaptation (UDA) has emerged as a fundamental approach to address cross-domain HSI classification challenges by leveraging labeled source domain data alongside unlabeled target domain samples during training [7, 14]. Early UDA methods for HSI classification focused on instance-based approaches that adjust the marginal distribution of source or target samples. Huang et al. [24] proposed the kernel mean matching (KMM) algorithm, which directly generates resampling weights by matching the distributions of training and testing sets in feature space without

estimating the distribution. Building upon this foundation, Li et al. [25] introduced the cost-sensitive self-paced learning (CSSPL) framework, which gradually trains from simple samples to complex samples through self-adjusting learning while automatically assigning different sample weights to select more reliable samples for training.

Feature-based UDA methods have gained significant attention by utilizing source and target domain data to find a common feature space through transformations, making data distributions more similar across domains. Sun et al. [26] proposed transfer sparse subspace analysis (TSSA) for cross-view scene model adaptation, focusing on transferring semantic scene knowledge from ground view images to high-resolution remote sensing images. More recently, Jia et al. [27] developed a gradient feature-oriented 3-D domain adaptation (GF-3DDA) approach for HSI classification, using 3-D Gabor filters to remove noise from original data and extending 2-D Sobel gradient and 2-D derivative-of-Gaussian to accommodate the spatial-spectral organization of HSIs. Zhou and Shi [28] proposed a deep adapted feature alignment method for UDA, while Ren et al. [29] introduced a modified cycle generative adversarial network (CycleGAN) to achieve higher accuracy and stability.

Deep UDA methods have revolutionized cross-domain HSI classification by leveraging the powerful representation capabilities of deep neural networks. Zhu et al. [30] proposed the deep subdomain adaptation network (DSAN) to expand feature representation capabilities by aligning distributions of relevant subdomains in multiple domain-specific layers. Li et al. [31] developed a two-stage deep domain adaptation method for HSI classification to learn more discriminative deep embedding spaces and minimize data differences between domains. Huang et al. [15] introduced the two-branch attention adversarial domain adaptation network, while Chen et al. [32] proposed supervised contrastive learning-based UDA (SCLUDA) that performs supervised contrastive learning in both source and target domains simultaneously to reduce within-class distance and increase between-class distance.

Recent advances in deep UDA have focused on addressing specific challenges in HSI classification, such as distribution alignment and feature discriminability. Liu et al. [12] proposed class-wise distribution adaptation for unsupervised classification of hyperspectral remote sensing images, while Wang et al. [9] developed joint correlation alignment-based graph neural networks for domain adaptation of multitemporal hyperspectral remote sensing images. Ma et al. [8] introduced cross-dataset hyperspectral image classification based on adversarial domain adaptation, and Mdrafai et al. [13] proposed attention-based domain adaptation using residual networks. More recently, Chen et al. [33] developed decoupled contrastive learning-based unsupervised domain adaptation (DCLUDA) that introduces a unique DA loss specifically designed to minimize class confusion in the target domain while employing decoupled contrastive learning to enhance data separability within each domain.

2.2 Domain Generalization for HSI Classification

Domain generalization (DG) represents a more challenging yet practical paradigm that aims to learn domain-invariant representations from source domains alone, enabling direct application to unseen target domains without requiring any target data during training [20, 21]. The field of domain generalization for HSI classification has witnessed significant developments in recent years, with researchers proposing various strategies to address the fundamental challenge of domain shift across different imaging conditions and geographical locations.

One of the pioneering works in this area was introduced by Peng et al. [20], who proposed a Disentanglement-Inspired Single-Source Domain Generalization Network (DSDGnet) for cross-scene HSI classification. This method identifies that extracting latent domain-invariant representation (DIR) of HSI could potentially mitigate spectral heterogeneity issues. The approach employs a style transfer module based on a Transformer encoder-transfer-decoder to expand the single source domain to an extended domain, followed by disentanglement of domain-invariant and domain-specific features. Wang et al. [21] subsequently proposed a dual-attention deep discriminative domain generalization framework (DAD3GM) that incorporates dual-attention feature learning (DAFL) and deep discriminative feature learning (DDFL) modules. The DAFL module extracts spatial features through multi-scale self-attention and spectral features through multi-head external attention, while DDFL enhances discriminative capability across domains.

Recent advances in domain generalization have focused on incorporating theoretical foundations and novel architectural designs. Gao et al. [34] introduced the Convergence and Error-Constrained Conditional Domain Generalization method (C³DG) for hyperspectral imagery classification, which relies solely on spectral information to solve the hyperspectral-monospectra problem. The method incorporates convergence and constrained-risk theories to provide theoretical support for model stability and generalization performance. Wang et al. [23] proposed a two-stage domain alignment single-source domain generalization network that generates simulated images to enhance model generalization ability while utilizing supervised contrastive learning to prevent redundant learning.

The integration of semantic information and causal reasoning has emerged as another important direction in domain generalization for HSI classification. Wang et al. [22] developed an explicit high-level semantic network (EHSnet) that leverages multilayered explicit high-level semantic information from different types of texts to provide precisely

relevant semantic information for image encoders, addressing domain shift problems by improving generalization capability through image-text alignment. Additionally, researchers have explored causal invariance approaches, where causal relationships are assumed to reflect the effects of changes in class information and domain information on samples, leading to networks that separate class-related and domain-related features [35].

The evolution of domain generalization methods has also been influenced by advances in transformer architectures and attention mechanisms. Recent works have demonstrated that transformer-based approaches can effectively capture long-range dependencies and cross-domain relationships, making them particularly suitable for HSI classification tasks where spectral and spatial information must be jointly considered across different domains [36]. These developments have established domain generalization as a viable alternative to domain adaptation, particularly in scenarios where target domain data is unavailable during training.

2.3 Open-Set Recognition for HSI Classification

Open-set recognition (OSR) addresses the challenge of identifying unknown classes that were not present during training, which is crucial for real-world HSI classification applications where new land cover types may emerge or be encountered in different geographical regions [37, 38]. Traditional HSI classification methods assume a closed-world scenario where all possible classes are known during training, but this assumption often fails in practical deployments where novel classes or unexpected land cover changes occur.

Early approaches to open-set recognition in HSI classification were primarily based on discriminative models that aim to learn decision boundaries for known classes while rejecting samples that fall outside these boundaries. Scheirer et al. [37] defined the open-set classification problem as a constrained minimization problem and added open space risk terms in the modeling process to evaluate the risk of samples belonging to known classes. Building upon this foundation, Bendale and Boulton [39] introduced OpenMax, which calibrates the SoftMax probability for each class using a Weibull distribution model, representing one of the first attempts to apply deep networks to open-set recognition.

The application of extreme value theory (EVT) has proven particularly effective for HSI open-set recognition. Liu et al. [40] proposed a multitask deep learning method for open-set classification of HSI that simultaneously learns classification and reconstruction during training. Based on extreme value theory, the method achieves identification of unknown samples by analyzing reconstruction errors, operating under the assumption that known classes can be accurately reconstructed while unknown classes cannot. This approach has been extended to few-shot scenarios, where Yue et al. [41] proposed spectral-spatial latent reconstruction for open-set HSI that simultaneously learns spectral feature reconstruction, spatial feature reconstruction, and pixel-level classification to obtain more robust open-set classification models.

Generative model-based approaches have emerged as another important direction for open-set recognition in HSI classification. These methods typically employ generative adversarial networks (GANs) or autoencoders to model the distribution of known classes and identify unknown samples based on their inability to be properly generated or reconstructed. Ge et al. [42] extended OpenMax to Generative OpenMax (G-OpenMax) by introducing GANs, where the generator generates synthetic samples of new classes and the discriminator learns explicit representations of unknown classes. More recently, researchers have explored the combination of OSR with domain adaptation specifically for HSI classification, leading to the development of open-set domain adaptation methods.

Recent advances in OSR for HSI have focused on addressing the specific challenges posed by hyperspectral data, including high dimensionality, spectral variability, and limited labeled samples. Pal et al. [43] proposed a few-shot open-set recognition method for HSIs with an outlier calibration network, using outlier calibration to reject unknown classes while introducing a feature enhancement paradigm to estimate the distribution of known classes. The method addresses the challenge of limited training samples that is particularly pronounced in hyperspectral applications. Sun et al. [44] further developed a spectral-spatial multiple layer perceptron (MLP)-like network to extract more discriminative features and introduced reciprocal points learning to classify between known and unknown classes, demonstrating the importance of joint spectral-spatial feature learning for effective open-set recognition.

The few-shot open-set recognition (FSOSR) paradigm has gained particular attention in the HSI community due to the inherent challenge of obtaining sufficient labeled samples for all land cover classes. This approach recognizes that several land cover classes may have limited training data, making it difficult to approximate their distributions accurately. Recent developments in this area have focused on meta-learning approaches that can quickly adapt to new tasks with limited data while maintaining the ability to reject unknown classes [45].

2.4 Open-Set Domain Adaptation for HSI Classification

Open-set domain adaptation (OSDA) combines the challenges of domain shift and unknown class detection, representing a more realistic scenario for practical HSI classification applications where target domains may contain both known classes with different distributions and entirely unknown classes [17, 18]. This paradigm recognizes that traditional domain adaptation methods may fail catastrophically when unknown classes are present in the target domain, as they attempt to align unknown target samples with known source classes, leading to negative transfer phenomena.

The foundational work in OSDA was established by Saito et al. [17], who proposed open-set backpropagation (OSBP) based on reverse propagation, using a generative model to address the DA problem without exploring domain information but enforcing hard thresholds. This approach highlighted the fundamental challenge that direct domain alignment can lead to negative transfer when unknown classes are present. Liu et al. [46] subsequently proposed the separate to adapt (STA) method that relies solely on source training classifier decisions to separate unknown target samples, though this approach may provide uncertain predictions for target samples due to domain shift effects.

More sophisticated OSDA methods have emerged that incorporate weighting mechanisms and uncertainty quantification to address negative transfer. Shermin et al. [18] proposed adversarial DA with multiple auxiliary classifiers (DAMCs), introducing a weighting module that assigns weights to target samples representing their likelihood of belonging to known versus unknown classes. This encourages positive transfer during adversarial training while reducing the domain gap between shared classes. Chang et al. [47] developed the mutual separation (MTS) method using deep mutual learning, which alternately trains a sample separation network and a distribution matching network to separate unknown samples and match inter-domain distributions.

Recent developments in OSDA for HSI classification have focused on addressing the specific challenges posed by hyperspectral data characteristics. Bi et al. [19] proposed weighted generative adversarial networks and dynamic thresholding (WGDT) specifically for HSI classification, introducing a class anchor (CA) strategy to learn the metric space of known classes in the source domain. By calculating similarity between target-domain samples and CAs, the method computes reliability weights for samples belonging to known classes, enabling instance-level weighted-domain adversarial learning to better align samples more likely to belong to known classes while avoiding negative transfer.

The integration of uncertainty quantification and adaptive thresholding has emerged as a key trend in OSDA for HSI. Jang et al. [48] proposed unknown-aware domain adversarial learning (UADAL), which aligns known distributions of source and target while separating unknown target distributions in the feature alignment process. Ru et al. [49] introduced open-set moving-threshold estimation and gradual alignment (OMEGA) to address problems of intra-domain class imbalance and inter-domain label shift, while Li et al. [50] proposed adjustment and alignment (ANNA) for unbiased OSDA, using front-door adjustment to find novel classes hidden in base-class images to correct biased learning in the source domain.

The field has also seen exploration of source-free scenarios, where target domain adaptation must be performed without access to source domain data during adaptation. Wan et al. [51] focused on knowledge transfer without access to source-domain data and proposed open-set source-free DA (OS-SFDA), using an unknown diffuser to explore more accurate class spaces and employing reliable known knowledge with clustering pseudo-labels to achieve effective known knowledge transfer and unknown generalization. This direction addresses practical scenarios where source data cannot be shared due to privacy or security constraints, which is particularly relevant for HSI applications involving sensitive geographical or military information.

2.5 Evidential Learning for HSI Classification

Evidential learning represents a principled framework for uncertainty quantification that models the predictive distribution using higher-order probability distributions, enabling simultaneous prediction and uncertainty estimation crucial for robust open-set and domain adaptation scenarios [52, 53]. This paradigm has emerged as a fundamental approach to address the inherent uncertainty challenges in hyperspectral image classification, particularly when dealing with unknown classes or domain shifts where traditional confidence measures prove insufficient.

Early applications of evidential learning focused on standard classification tasks with uncertainty quantification. Sensoy et al. [52] introduced the foundational evidential deep learning framework, which places a Dirichlet distribution over the class probabilities and treats the network outputs as evidence for this distribution. This approach provides both predictive probabilities and epistemic uncertainty estimates, making it particularly suitable for identifying out-of-distribution samples. Building upon this foundation, Joo and Kang [53] proposed being Bayesian about categorical distributions, extending the framework to handle various uncertainty types in classification tasks.

The integration of evidential learning with open-set recognition has gained significant attention due to its natural ability to quantify prediction uncertainty. Zhao et al. [54] developed uncertainty-guided continual learning methods that

leverage evidential learning principles to identify novel classes while maintaining performance on known classes. More recently, Choi et al. [55] proposed evidential deep learning for open-set action recognition, demonstrating that the framework’s uncertainty estimates can effectively distinguish between known and unknown action categories. Chen et al. [56] extended this approach to multi-label classification scenarios, showing improved performance in identifying unknown label combinations.

For domain adaptation applications, evidential learning has proven effective in handling domain-specific uncertainties. Hu et al. [57] proposed evidential domain adaptation networks that utilize uncertainty estimates to weight the importance of source and target domain samples during adaptation. The method employs evidential learning to quantify both aleatoric and epistemic uncertainties, enabling more robust domain alignment. Li et al. [58] developed an uncertainty-aware domain adaptation for medical image analysis, utilizing evidential learning to identify reliable pseudolabels in the target domain while rejecting uncertain predictions.

Recent advances in evidential learning for domain generalization have focused on learning domain-invariant representations with uncertainty awareness. Wang et al. [59] proposed evidential domain generalization networks that learn to predict both class labels and domain-specific uncertainties, enabling better generalization to unseen domains. The approach uses evidential learning to model the uncertainty over domain-invariant features, improving robustness across different domains. Kumar et al. [60] introduced uncertainty-guided domain generalization for semantic segmentation, demonstrating that evidential learning can identify regions where domain-specific adaptations are needed.

The application of evidential learning to hyperspectral image analysis has emerged as a promising research direction. Zhang et al. [61] proposed evidential learning for hyperspectral image classification under distribution shift, utilizing the framework’s uncertainty quantification capabilities to identify spectral regions affected by atmospheric or sensor variations. More recently, Liu et al. [62] developed spectral-spatial evidential networks for hyperspectral open-set recognition, combining evidential learning with attention mechanisms to capture spectral and spatial information through a unified uncertainty estimation framework. The method demonstrates superior performance in identifying unknown land cover types while maintaining high accuracy in known classes.

The integration of evidential learning with self-supervised learning has opened new avenues for unsupervised domain adaptation. Yang et al. [63] proposed self-supervised evidential learning for domain adaptation, where the model learns to predict both semantic labels and domain-specific uncertainties without requiring target domain labels. This approach has shown particular promise for hyperspectral applications where labeled target domain data are often unavailable. Furthermore, evidential learning has been combined with meta-learning approaches for few-shot domain adaptation, enabling rapid adaptation to new domains with limited data while maintaining uncertainty awareness [64].

3 Proposed method

3.1 Architecture overview

The proposed method consists of four main components:

1. **Spectrum-Invariant Frequency Disentanglement (SIFD)**: Domain generalization module
2. **Dual-Channel Residual Network (DCRN)**: Spectral-spatial feature extraction
3. **Evidential Deep Learning (EDL)**: Uncertainty quantification
4. **Spectral-Spatial Uncertainty Disentanglement (SSUD)**: Open-set classification

The overall architecture can be expressed as:

$$\begin{cases} \mathbf{x}_{inv} &= \text{SIFD}(\mathbf{x}) \\ \mathbf{x}_{enh} &= \mathbf{x} + \alpha \cdot \mathbf{x}_{inv} \\ \{\mathbf{f}_{spec}, \mathbf{f}_{spat}, \mathbf{f}_{comb}\} &= \text{DCRN}(\mathbf{x}_{enh}) \\ \{\mathbf{u}_{spec}, \mathbf{u}_{spat}, \mathbf{u}_{comb}\} &= \text{EDL}(\{\mathbf{f}_{spec}, \mathbf{f}_{spat}, \mathbf{f}_{comb}\}) \\ \hat{y} &= \text{SSUD}(\mathbf{u}_{spec}, \mathbf{u}_{spat}, \mathbf{u}_{comb}) \end{cases} \quad (1)$$

where:

- $\mathbf{x} \in \mathbb{R}^{H \times W \times C}$: input hyperspectral image with height H , width W , and C spectral bands
- $\mathbf{x}_{inv} \in \mathbb{R}^{H \times W \times C}$: domain-invariant features extracted by SIFD
- α : fusion weight for combining original and invariant features

- $\mathbf{x}_{enh} \in \mathbb{R}^{H \times W \times C}$: enhanced input combining original and invariant features
- $\mathbf{f}_{spec}, \mathbf{f}_{spat}, \mathbf{f}_{comb} \in \mathbb{R}^D$: spectral, spatial, and combined feature vectors of dimension D
- $\mathbf{u}_{spec}, \mathbf{u}_{spat}, \mathbf{u}_{comb} \in [0, 1]$: uncertainty measures for spectral, spatial, and combined pathways
- $\hat{y} \in \{1, 2, \dots, K, \text{unknown}\}$: predicted class label including unknown class

Hyperspectral images from different domains exhibit domain-specific variations due to acquisition conditions, sensor differences, and environmental factors. The proposed framework addresses this challenge by first extracting domain-invariant spectral features through the SIFD module, which operates in the frequency domain to identify robust spectral characteristics. The enhanced input combines original spectral information with these invariant features to preserve essential spectral signatures while improving cross-domain generalization. Subsequently, the DCRN processes the enhanced input through parallel spectral and spatial pathways to capture complementary feature representations. The EDL module then quantifies uncertainty for each pathway using evidential learning principles, providing reliable confidence estimates for the extracted features. Finally, the SSUD module performs open-set classification by disentangling spectral and spatial uncertainties to distinguish between known and unknown classes across different domains. The complete framework is illustrated in Figure 1.

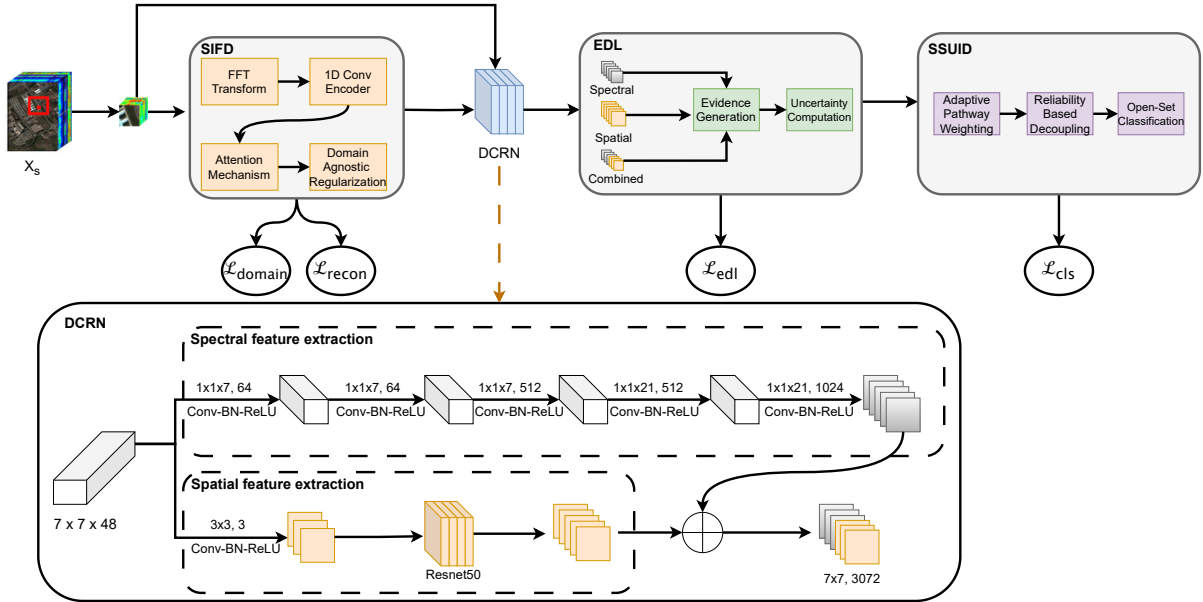


Figure 1: Illustration of the proposed open-set domain generalization framework. The architecture consists of four main components: SIFD for domain-invariant feature extraction, DCRN for spectral-spatial feature learning, EDL for uncertainty quantification, and SSUID for open-set classification. The detailed DCRN module shows parallel spectral and spatial feature extraction pathways that are fused to generate multi-scale representations. The arrows indicate the data flow through the network. The loss functions \mathcal{L}_{domain} , \mathcal{L}_{recon} , \mathcal{L}_{edl} , and \mathcal{L}_{cls} are computed at their respective modules and combined for end-to-end training. The numbers in the blocks indicate the spatial and channel dimensions (height×width×channels) of feature maps throughout the convolutional layers.

3.2 Spectrum-Invariant Frequency Disentanglement (SIFD)

3.2.1 Motivation

Hyperspectral images from different domains (temporal, geographical) exhibit domain-specific spectral variations due to atmospheric conditions, sensor differences, and environmental factors. SIFD addresses this by extracting domain-invariant spectral features in the frequency domain.

3.2.2 Frequency Domain Transformation

For each pixel spectrum $\mathbf{s} \in \mathbb{R}^C$, we compute the discrete Fourier transform:

$$\begin{cases} \mathbf{S}_{complex} = \text{FFT}(\mathbf{s}) \\ \mathbf{S}_{real} = \Re(\mathbf{S}_{complex}) \\ \mathbf{S}_{imag} = \Im(\mathbf{S}_{complex}) \\ \mathbf{S}_{freq} = [\mathbf{S}_{real}; \mathbf{S}_{imag}] \in \mathbb{R}^{2 \times (C/2+1)} \end{cases} \quad (2)$$

where:

- $\mathbf{s} \in \mathbb{R}^C$: pixel spectrum vector containing C spectral band values
- $\mathbf{S}_{complex} \in \mathbb{C}^{C/2+1}$: complex-valued Fourier coefficients
- $\mathbf{S}_{real}, \mathbf{S}_{imag} \in \mathbb{R}^{C/2+1}$: real and imaginary parts of Fourier coefficients
- $\mathbf{S}_{freq} \in \mathbb{R}^{2 \times (C/2+1)}$: concatenated real and imaginary frequency features

3.2.3 Invariant Feature Extraction

The frequency features are processed through a 1D convolutional encoder:

$$\begin{cases} \mathbf{F}_{freq} = \text{Conv1D}_{64}(\text{ReLU}(\text{BN}(\text{Conv1D}_{32}(\mathbf{S}_{freq})))) \\ \mathbf{F}_{inv} = \text{Conv1D}_{64}(\text{ReLU}(\text{BN}(\mathbf{F}_{freq}))) \end{cases} \quad (3)$$

where:

- $\mathbf{F}_{freq} \in \mathbb{R}^{64}$: intermediate frequency features with 64 channels
- $\mathbf{F}_{inv} \in \mathbb{R}^{64}$: domain-invariant features in frequency domain
- Conv1D_n : 1D convolution layer with n output channels
- BN: Batch Normalization layer
- ReLU: Rectified Linear Unit activation function

An attention mechanism identifies the most domain-invariant frequency components:

$$\begin{cases} \mathbf{A} = \sigma(\text{Conv1D}_1(\text{AdaptiveAvgPool1D}(\mathbf{F}_{inv}))) \\ \mathbf{F}_{att} = \mathbf{F}_{inv} \odot \mathbf{A} \end{cases} \quad (4)$$

where:

- $\mathbf{A} \in [0, 1]^{64}$: attention weights for each feature channel
- σ : sigmoid activation function
- \odot : element-wise multiplication
- $\mathbf{F}_{att} \in \mathbb{R}^{64}$: attention-weighted invariant features

3.2.4 Domain-Agnostic Regularization

Instead of traditional domain adversarial training, we employ domain-agnostic regularization:

$$\begin{cases} \mathbf{d} = \text{GRL}_\lambda(\text{AdaptiveAvgPool1D}(\mathbf{F}_{att})) \\ \mathbf{p}_{domain} = \text{MLP}(\mathbf{d}) \\ \mathcal{L}_{domain} = \text{BCE}(\mathbf{p}_{domain}, 0.5) \end{cases} \quad (5)$$

where:

- $\mathbf{d} \in \mathbb{R}^{64}$: domain features after gradient reversal
- GRL_λ : Gradient Reversal Layer with reversal strength λ

- $\lambda \in \mathbb{R}^+$: gradient reversal strength parameter controlling adversarial training intensity
- $\mathbf{p}_{domain} \in [0, 1]$: predicted domain probability
- \mathcal{L}_{domain} : binary cross-entropy loss encouraging domain-neutral predictions

To ensure information preservation, we reconstruct the original spectrum:

$$\begin{cases} \mathbf{s}_{recon} &= \sigma(\text{MLP}(\text{AdaptiveAvgPool1D}(\mathbf{F}_{att}))) \\ \mathcal{L}_{recon} &= \|\mathbf{s} - \mathbf{s}_{recon}\|_2^2 \end{cases} \quad (6)$$

where:

- $\mathbf{s}_{recon} \in \mathbb{R}^C$: reconstructed spectrum
- \mathcal{L}_{recon} : mean squared error reconstruction loss
- $\|\cdot\|_2^2$: squared L2 norm

3.3 Dual-Channel Residual Network (DCRN)

3.3.1 Motivation

Hyperspectral images contain rich information in both spectral and spatial dimensions that provide complementary discriminative features. However, existing methods often process these modalities independently or through simple concatenation, failing to capture their inherent correlations. DCRN addresses this limitation by designing specialized pathways for spectral and spatial feature extraction, followed by attention-based fusion to leverage the strengths of both modalities.

3.3.2 Spectral Pathway

The spectral pathway uses 1D convolutions to capture spectral patterns:

$$\begin{cases} \mathbf{F}_{s1} &= \text{ReLU}(\text{BN}(\text{Conv2D}_{64}^{1 \times 7}(\mathbf{x}))) \\ \mathbf{F}_{s2} &= \text{ReLU}(\text{BN}(\text{Conv2D}_{64}^{1 \times 7}(\mathbf{F}_{s1}))) \\ \mathbf{F}_{s3} &= \text{ReLU}(\text{BN}(\text{Conv2D}_{512}^{1 \times 7}(\mathbf{F}_{s2}))) \\ \mathbf{F}_{s4} &= \text{ReLU}(\text{BN}(\text{Conv2D}_{512}^{1 \times 21}(\mathbf{F}_{s3}))) \\ \mathbf{F}_{spec} &= \text{ReLU}(\text{BN}(\text{Conv2D}_{1024}^{1 \times 21}(\mathbf{F}_{s4}))) \end{cases} \quad (7)$$

where:

- $\text{Conv2D}_{out}^{h \times w}$: 2D convolution with out output channels and kernel size $h \times w$
- $\mathbf{F}_{s1}, \mathbf{F}_{s2} \in \mathbb{R}^{H \times W \times 64}$: first two spectral feature maps
- $\mathbf{F}_{s3}, \mathbf{F}_{s4} \in \mathbb{R}^{H \times W \times 512}$: intermediate spectral feature maps
- $\mathbf{F}_{spec} \in \mathbb{R}^{H \times W \times 1024}$: final spectral features

3.3.3 Spatial Pathway

The spatial pathway employs ResNet50 backbone for spatial context:

$$\begin{cases} \mathbf{F}_{sp1} &= \text{ReLU}(\text{BN}(\text{Conv2D}_3^{3 \times 3}(\mathbf{x}))) \\ \mathbf{F}_{sp2} &= \text{ResNet50Adapter}(\mathbf{F}_{sp1}) \\ \mathbf{F}_{sp3} &= \text{ResNet50Layer1}(\mathbf{F}_{sp2}) \\ \mathbf{F}_{sp4} &= \text{ResNet50Layer2}(\mathbf{F}_{sp3}) \\ \mathbf{F}_{sp5} &= \text{ResNet50Layer3}(\mathbf{F}_{sp4}) \\ \mathbf{F}_{spat} &= \text{Upsample}(\text{ResNet50Layer4}(\mathbf{F}_{sp5})) \end{cases} \quad (8)$$

where:

- $\mathbf{F}_{sp1} \in \mathbb{R}^{H \times W \times 3}$: RGB-like representation for ResNet input
- $\mathbf{F}_{sp2}, \dots, \mathbf{F}_{sp5}$: intermediate spatial features from ResNet layers
- $\mathbf{F}_{spat} \in \mathbb{R}^{H \times W \times 2048}$: final spatial features

3.3.4 Feature Fusion with Attention

The spectral and spatial features are fused using channel and spatial attention:

$$\begin{cases} \mathbf{F}_{fused} &= \text{Conv2D}_{3072}^{1 \times 1}([\mathbf{F}_{spec}; \mathbf{F}_{spat}]) \\ \mathbf{A}_{channel} &= \sigma(\text{MLP}(\text{GAP}(\mathbf{F}_{fused}) + \text{GMP}(\mathbf{F}_{fused}))) \\ \mathbf{F}_{ca} &= \mathbf{F}_{fused} \odot \mathbf{A}_{channel} + \gamma_{res} \cdot \mathbf{F}_{fused} \\ \mathbf{A}_{spatial} &= \sigma(\text{Conv2D}_1^{7 \times 7}([\text{AvgPool}(\mathbf{F}_{ca}); \text{MaxPool}(\mathbf{F}_{ca})])) \\ \mathbf{F}_{final} &= \mathbf{F}_{ca} \odot \mathbf{A}_{spatial} + \gamma_{res} \cdot \mathbf{F}_{ca} \end{cases} \quad (9)$$

where:

- $\mathbf{F}_{fused} \in \mathbb{R}^{H \times W \times 3072}$: concatenated spectral and spatial features
- $\mathbf{A}_{channel} \in [0, 1]^{3072}$: channel attention weights
- $\mathbf{F}_{ca} \in \mathbb{R}^{H \times W \times 3072}$: channel-attention weighted features
- $\mathbf{A}_{spatial} \in [0, 1]^{H \times W \times 1}$: spatial attention map
- $\mathbf{F}_{final} \in \mathbb{R}^{H \times W \times 3072}$: final fused features
- γ_{res} : residual connection weight
- GAP and GMP denote global average and global max pooling respectively.

3.4 Evidential Deep Learning (EDL) for Uncertainty Quantification

3.4.1 Motivation

Traditional deep learning models provide point estimates without quantifying prediction uncertainty, which is crucial for open-set scenarios where unknown classes may be encountered. EDL addresses this limitation by modeling the predictive distribution using a Dirichlet distribution, enabling the network to express uncertainty about its predictions.

3.4.2 Evidence Generation

For each pathway (spectral, spatial, combined), we generate evidence:

$$\begin{cases} \mathbf{e}_i &= \max(0, \text{Linear}(\mathbf{f}_i)) + \epsilon \\ \boldsymbol{\alpha}_i &= \mathbf{e}_i + 1 \end{cases} \quad (10)$$

where:

- $\mathbf{e}_i \in \mathbb{R}^K$: evidence vector for pathway i
- ϵ : small constant for numerical stability
- $i \in \{\text{spec}, \text{spat}, \text{comb}\}$: pathway index
- $\boldsymbol{\alpha}_i \in \mathbb{R}^K$: Dirichlet distribution parameters
- K : total number of known classes

3.4.3 Uncertainty Computation

The uncertainty for each pathway is computed as:

$$\begin{cases} S_i &= \sum_{k=1}^K \alpha_{i,k} \\ \mathbf{p}_i &= \frac{\boldsymbol{\alpha}_i}{S_i} \\ u_i &= \frac{K}{S_i} \end{cases} \quad (11)$$

where:

- $S_i \in \mathbb{R}^+$: Dirichlet strength (sum of parameters)
- $\mathbf{p}_i \in [0, 1]^K$: expected probability distribution over classes
- $u_i \in [0, 1]$: uncertainty measure (higher values indicate more uncertainty)

The EDL loss combines mean squared error with regularization:

$$\begin{cases} \mathbf{y}_{onehot} &= \text{OneHot}(y, K) \\ \mathcal{L}_{MSE} &= ||\mathbf{y}_{onehot} - \mathbf{p}_i||_2^2 \\ \mathcal{L}_{reg} &= \sum_{k=1}^K (1 - y_{onehot,k}) \cdot \alpha_{i,k} \\ \mathcal{L}_{EDL} &= \mathcal{L}_{MSE} + \lambda_{reg} \cdot \mathcal{L}_{reg} \end{cases} \quad (12)$$

where:

- $y \in \{1, \dots, K\}$: true class label
- $\mathbf{y}_{onehot} \in \{0, 1\}^K$: one-hot encoded label vector
- \mathcal{L}_{MSE} : mean squared error between predicted and true distributions
- \mathcal{L}_{reg} : regularization term penalizing evidence for incorrect classes
- λ_{reg} : regularization weight

3.5 Spectral-Spatial Uncertainty Disentanglement (SSUD)

3.5.1 Motivation

Different feature modalities (spectral vs. spatial) may exhibit varying reliability across different samples and domains. SSUD addresses this by disentangling uncertainties from different pathways and adaptively weighting their contributions based on reliability.

3.5.2 Adaptive Pathway Weighting

The relative reliability of spectral and spatial pathways is determined adaptively:

$$\begin{cases} \mathbf{w} &= \text{Softmax}(\text{MLP}([\mathbf{f}_{spec}; \mathbf{f}_{spat}])) \\ u_{weighted} &= w_1 \cdot u_{spec} + w_2 \cdot u_{spat} \end{cases} \quad (13)$$

where:

- $\mathbf{w} = [w_1, w_2] \in [0, 1]^2$: pathway weights with $w_1 + w_2 = 1$
- $[\mathbf{f}_{spec}; \mathbf{f}_{spat}]$: concatenated spectral and spatial features
- $u_{weighted} \in [0, 1]$: weighted uncertainty combining both pathways

3.5.3 Reliability-Based Decoupling

Reliability scores are computed as the inverse of uncertainty:

$$\begin{cases} r_{spec} &= 1 - u_{spec} \\ r_{spat} &= 1 - u_{spat} \\ \Delta r &= |r_{spec} - r_{spat}| \end{cases} \quad (14)$$

where:

- $r_{spec}, r_{spat} \in [0, 1]$: reliability scores for spectral and spatial pathways
- $\Delta r \in [0, 1]$: reliability difference between pathways

When $\Delta r > \tau_{decouple}$, the system uses pathway-specific uncertainty:

$$u_{final} = \begin{cases} \max(u_{spec}, \gamma_{down} \cdot u_{spat}) & \text{if } r_{spec} > r_{spat} \\ \max(u_{spat}, \gamma_{down} \cdot u_{spec}) & \text{if } r_{spat} > r_{spec} \\ u_{combined} & \text{otherwise} \end{cases} \quad (15)$$

where:

- $u_{final} \in [0, 1]$: final uncertainty measure
- $\tau_{decouple}$: threshold for pathway decoupling
- γ_{down} : down-weighting factor for less reliable pathway
- $u_{combined}$: uncertainty from the combined pathway

3.5.4 Open-Set Classification

The final classification decision uses a rejection score:

$$\begin{cases} \mathbf{p}_{cls} &= \text{Softmax}(\text{MLP}(\mathbf{f}_{combined})) \\ p_{max} &= \max(\mathbf{p}_{cls}) \\ \hat{k} &= \arg \max(\mathbf{p}_{cls}) \\ r_{score} &= \omega_{spec} \cdot u_{final} + \omega_{prob} \cdot (1 - p_{max}) \\ \hat{y} &= \begin{cases} \hat{k} & \text{if } r_{score} \leq \tau \\ \text{unknown} & \text{otherwise} \end{cases} \end{cases} \quad (16)$$

where:

- $\mathbf{p}_{cls} \in [0, 1]^K$: class probability distribution
- $p_{max} \in [0, 1]$: maximum probability (confidence)
- $\hat{k} \in \{1, \dots, K\}$: predicted class index
- $r_{score} \in [0, 2]$: rejection score combining uncertainty and confidence
- ω_{spec} : weight for spectral uncertainty
- ω_{prob} : weight for probability-based uncertainty
- τ : rejection threshold
- \hat{y} : final prediction including unknown option

3.6 Training Strategy

3.6.1 Motivation

Training a multi-component architecture with diverse objectives requires careful balance between different loss terms and training strategies. The framework must simultaneously learn domain-invariant features, extract discriminative spectral-spatial representations, quantify uncertainties, and perform classification.

3.6.2 Loss Function

The complete training loss combines multiple objectives:

$$\mathcal{L}_{total} = \mathcal{L}_{cls} + \alpha \mathcal{L}_{EDL} + \beta \mathcal{L}_{domain} + \gamma \mathcal{L}_{recon} \quad (17)$$

where:

- $\mathcal{L}_{cls} = \text{CrossEntropy}(\mathbf{p}_{cls}, y)$: standard classification loss
- \mathcal{L}_{EDL} : combined evidential loss
- \mathcal{L}_{domain} : domain-agnostic regularization loss from SIFD
- \mathcal{L}_{recon} : spectrum reconstruction loss from SIFD
- α : weight for EDL loss
- β : weight for domain regularization
- γ : weight for reconstruction loss

3.6.3 Training Algorithm

The training procedure follows a structured approach to optimize all components simultaneously. The model is trained end-to-end using the Adam optimizer with an initial learning rate. During each training iteration, the SIFD module first extracts domain-invariant features, which are then combined with the original input to create enhanced representations. The DCRN processes these enhanced features through parallel spectral and spatial pathways, generating multi-scale feature representations. The EDL module computes uncertainty estimates for each pathway, while the SSUD module performs final classification decisions based on reliability-weighted uncertainties.

Gradient clipping with a maximum norm is applied to ensure stable training, particularly important given the multiple loss components. The training progresses for a specified number of epochs, with periodic validation to monitor convergence. After training completion, threshold calibration is performed using synthetic unknown samples to optimize rejection thresholds for open-set scenarios.

Algorithm 1 Training Algorithm

Input:

- Source domain dataset $D^s = \{(x_1^s, y_1^s), \dots, (x_{n^s}^s, y_{n^s}^s)\}$.
- Hyperparameters α, β, γ .
- Training epochs E .
- Target unknown rejection rate ρ_{target} .
- Randomly initialized model parameters $\theta_{SIFD}, \theta_{DCRN}, \theta_{EDL}$ and θ_{SSUD} .

Output:

- Model parameters after training.
- Calibrated threshold τ^* .

```

1: for epoch in  $E$  do
2:   for batch in dataloader do
3:     Extracting domain-invariant features  $x_{inv}$ 
4:     Enhanced input  $x_{enh}$ 
5:     Extract features  $\{f_{spec}, f_{spat}, f_{comb}\}$ 
6:     Compute uncertainties  $\{u_{spec}, u_{spat}, u_{comb}\}$ 
7:     Get class probabilities  $p_{cls}$ 
8:     Calculate classification loss  $L_{cls}$ 
9:     Calculate EDL loss  $L_{EDL}$ 
10:    Calculate domain loss  $L_{domain}$  and reconstruction loss  $L_{recon}$ 
11:     $L_{total} = L_{cls} + \alpha L_{EDL} + \beta L_{domain} + \gamma L_{recon}$ 
12:    Update parameters  $\theta_{SIFD}, \theta_{DCRN}, \theta_{EDL}, \theta_{SSUD}$ 
13:   end for
14: end for
15: Generate synthetic unknown samples using noise injection and class mixing
16: Calculate rejection scores for validation and synthetic samples
17: Optimize threshold  $\tau^*$ 

```

Algorithm 2 Testing Algorithm

Input:

- Target domain dataset $D^t = \{x_1^t, \dots, x_{n^t}^t\}$.
- Trained parameters $\theta_{SIFD}, \theta_{DCRN}, \theta_{EDL}$, and θ_{SSUD} .
- Calibrated threshold τ^* .

Output:

- Predicted values of the target domain dataset.

```

1: for batch in dataloader do
2:   Extracting target domain features  $x_{inv}$ 
3:   Enhanced input  $x_{enh}$ 
4:   Extract features  $\{f_{spec}, f_{spat}, f_{comb}\}$ 
5:   Compute uncertainties  $\{u_{spec}, u_{spat}, u_{comb}\}$ 
6:   Get class probabilities  $p_{cls}$ 
7:   Calculate rejection score  $r_{score}$ 
8:   if  $r_{score} > \tau^*$  then
9:      $\hat{y} = \text{unknown}$ 
10:  else
11:     $\hat{y} = \arg \max(p_{cls})$ 
12:  end if
13: end for

```

3.7 Threshold Calibration via Synthetic Unknown Generation

3.7.1 Motivation

Open-set classification performance critically depends on the rejection threshold, which determines the trade-off between correctly classifying known samples and rejecting unknown ones. Since true unknown samples from the target domain are unavailable during training, synthetic unknown generation provides a principled approach to calibrate thresholds.

3.7.2 Unknown Sample Generation

The following methods are used to generate unknown samples for threshold calibration:

Gaussian Noise Injection:

$$\mathbf{x}_{noise} = \mathbf{x} + \mathcal{N}(0, \sigma^2 \mathbf{I}) \quad (18)$$

where σ represents different noise levels.

Class Mixing:

$$\mathbf{x}_{mix} = \lambda \mathbf{x}_i + (1 - \lambda) \mathbf{x}_j \quad (19)$$

where λ is the mixing weight and $\mathbf{x}_i, \mathbf{x}_j$ are samples from different classes.

Spectral and Spatial Corruption: Random corruption of 20-30% of spectral bands and 2-3 spatial patches respectively.

The optimal threshold τ^* is selected using ROC analysis to achieve a target unknown rejection rate:

$$\tau^* = \arg \min_{\tau} |TPR(\tau) - \rho_{target}| \quad (20)$$

This approach ensures robust performance across diverse hyperspectral domains while maintaining computational efficiency through focused feature extraction and uncertainty-guided decision making.

4 Experiments

4.1 Datasets

In order to verify the effectiveness of the proposed method, six datasets were used for experiments, including Pavia University (PU), Pavia Center (PC), Houston2013 (HU13), Houston2018 (HU18), Dioni, and Loukia. In the experiments, these six datasets were combined into three OSDA classification tasks. The first task uses PU as the source domain and PC as the target domain. The second task uses HU13 as the source domain and HU18 as the target domain. The third task uses Dioni and Loukia as the source domain and target domain, respectively. For each source domain, we employ a stratified split where 80% of the labeled samples are used for training and 20% are reserved for validation to ensure robust model development and threshold calibration.

4.1.1 PU-PC

Pavia is an HSI collected by the ROSIS sensor in Pavia, Northern Italy, which contains two scenes of PU and PC. The spatial size of PU is 610×340 pixels, the spatial resolution is 1.3 m, and there are 115 bands in total. After removing the 12 bands that are seriously affected by noise, 103 bands remain. The spatial size of the PC is 1096×715 pixels, the spatial resolution is also 1.3 m, and 102 bands remain after processing. In the experiments, 102 bands common to both datasets were used. Select seven common classes as the known classes, and select a class (Tiles) in the target domain as the unknown class. The pseudo-color images and ground truth images of the PU-PC task are shown in Fig. 2. The number of samples in the PU-PC task is shown in Table 1.

4.1.2 HU13-HU18

The Houston dataset contains two scenes, HU13 and HU18. HU13 is an HSI collected by the ITERS CASI-1500 sensor. The collection time was 2013 in Houston, TX, USA, and its surrounding rural areas. The spatial size of the HSI is 349×1905 pixels, and the spatial resolution is 2.5 m and contains 144 bands. HU18 is also an HSI collected near Houston. It was a dataset used in the competition held by IEEE GRSS Data Fusion in 2018. The spatial size is 601×2384 pixels, the spatial resolution is 1 m, the wavelength range is from 380 to 1050 nm, and there are 48 bands in total. In the experiment, 48 bands common to the two datasets were used. Merge the evergreen trees and deciduous trees classes in HU18 into the trees class, so that the two domains have seven known classes, and select the remaining 12 classes in the

target domain as an unknown class. The pseudo-color images and ground truth images of the HU13-HU18 task are shown in Fig. 3. The number of samples in the HU13-HU18 task is shown in Table 2.

4.1.3 Dioni-Loukia

Dioni and Loukia obtained from the Hyperion sensor, carried by the National Aeronautics and Space Administration (NASA) Earth Observing 1 (EO-1) satellite. After processing, 176 bands remain. The spatial size of Dioni is 250×1376 pixels, and the spatial size of Loukia is 249×945 pixels. In the experiment, nine ground object classes were selected as known classes, and three classes (dense sclerophyllous vegetation, sparsely vegetated areas, and water) in the target domain were selected as an unknown class. The pseudo-color images and ground truth images of the Dioni-Loukia task are shown in Fig. 4. The number of samples in the Dioni-Loukia task is shown in Table 3.

Table 1: Class Distribution for Pavia University - Pavia Centre

No.	Class	Pavia U	Pavia C
1	Trees	3064	7598
2	Asphalt	6631	9248
3	Bricks	3682	2685
4	Bitumen	1330	7287
5	Meadows	18649	3090
6	Shadow	947	2863
7	Bare Soil	5029	6584
8	Unknown	-	42826
Total		39332	82181

Table 2: Class Distribution for Houston 2013-2018

No.	Class	Houston2013	Houston2018
1	Grass healthy	1449	9799
2	Grass stressed	1444	32502
3	Trees	1432	18576
4	Water	507	266
5	Residential buildings	1464	39794
6	Non-residential buildings	1435	223789
7	Road	1445	45793
8	Unknown	-	134125
Total		9176	504644

Table 3: Class Distribution for Dioni-Loukia

No.	Class	Dioni	Loukia
1	Dense Urban Fabric	1262	206
2	Mineral Extraction Sites	204	54
3	Non Irrigated Arable Land	614	426
4	Fruit Trees	150	79
5	Olive Groves	1768	1107
6	Coniferous Forest	361	422
7	Sparse Sclerophyllous Vegetation	6374	2361
8	Rocks and Sand	492	453
9	Coastal Water	398	421
10	Unknown	-	4788
Total		11623	10317

4.2 Setup

4.2.1 Training details

All experiments were conducted on a NVIDIA GeForce RTX 3090 GPU. The Adam optimizer [65] was employed for model training with an initial learning rate of 1×10^{-5} and weight decay of 1×10^{-5} . The learning rate was scheduled

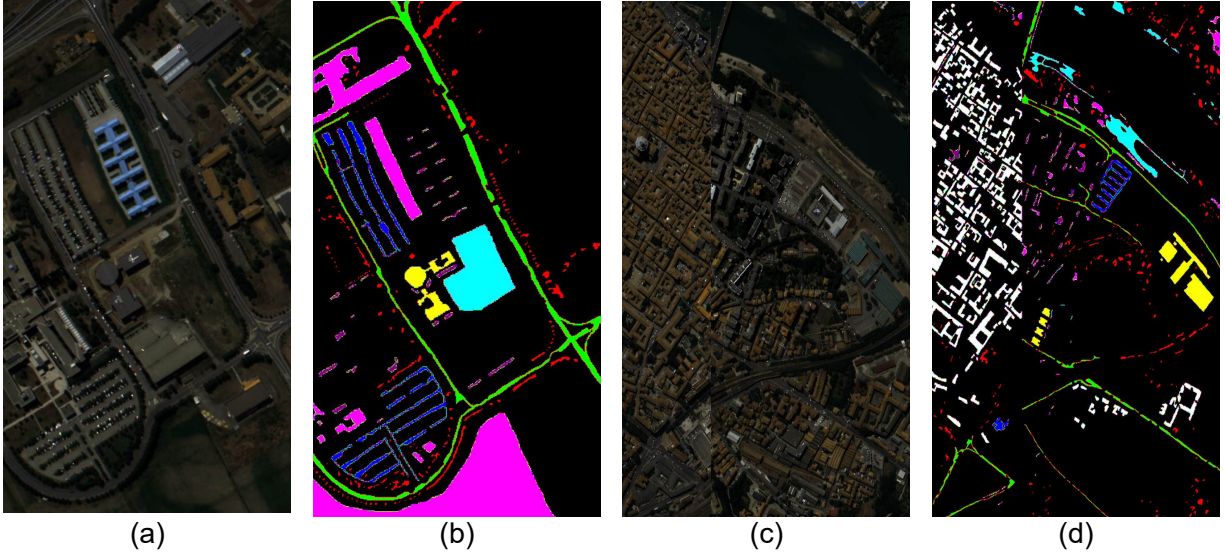


Figure 2: PU-PC task. (a) Pseudo-color image of PU. (b) Ground-truth image of PU. (c) Pseudo-color image of PC. (d) Ground-truth image of PC. **■** Background, **■** Brick, **■** Meadow, **■** Tree, **■** Bitumen, **■** Bare Soil, **■** Asphalt, **■** Shadow, **■** Unknown

using CosineAnnealingLR with T_{\max} equal to the total number of epochs and $\eta_{\min} = \text{lr}/10$. Training was conducted for 50 epochs with gradient clipping applied at a maximum norm of 1.0 to ensure training stability.

The input hyperspectral patches were set to $7 \times 7 \times C$ spatial-spectral cubes, where C represents the number of spectral bands (48 for Houston, 102 for Pavia, and 176 for Dioni-Loukia datasets). Batch size was set to 32 for all experiments.

The loss function combines multiple components with dataset-specific optimal weights determined through systematic hyperparameter tuning detailed in 4.6 Based on grid search analysis, for the Houston dataset, $\alpha = 0.3$ for EDL loss, $\beta = 0.7$ for domain adversarial loss, and $\gamma = 0.1$ for spectrum reconstruction loss. For the Pavia dataset, $\alpha = 0.9$, $\beta = 0.5$, and $\gamma = 0.1$. For the Dioni dataset, $\alpha = 0.9$, $\beta = 0.1$, and $\gamma = 0.3$. The regularization weight $\delta = 0.2$ and gradient reversal layer strength $\lambda = 1.0$ were kept constant across all experiments.

For the training strategy, a single-stage end-to-end approach was adopted where all components are trained jointly. After training completion, threshold calibration using outlier injection was performed targeting 75% unknown class rejection rate. The calibration employs multiple synthetic unknown generation strategies including Gaussian noise injection, class mixing, spectral corruption, and spatial corruption to optimize uncertainty thresholds.

The best model is selected based on validation accuracy, and final evaluation uses calibrated thresholds optimized through ROC analysis on synthetic unknown samples generated during the calibration phase.

4.2.2 Evaluation Metrics

To comprehensively evaluate the performance of our proposed method for open-set hyperspectral image classification, we employ several standard metrics that assess both closed-set accuracy and open-set detection capability.

Known Class Accuracy (OS): This metric measures the classification accuracy on known classes that appear in both source and target domains. It is calculated as:

$$\text{OS} = \frac{\text{Number of correctly classified known samples}}{\text{Total number of known samples}} \times 100\% \quad (21)$$

Unknown Class Rejection Rate (Unk): This metric evaluates the model’s ability to correctly identify and reject unknown class samples. It is defined as:

$$\text{Unk} = \frac{\text{Number of unknown samples correctly rejected}}{\text{Total number of unknown samples}} \times 100\% \quad (22)$$

Table 4: Classification Results on the PU-PC Task with the highest value highlighted in red and the second highest in blue.

Class	Domain Adaptation									Domain Generalization
	DACD	OSBP	DAMC	STA	MTS	UADAL	OMEGA	ANNA	WGDT	Ours
1	93.2	95.6	93.3	80.0	91.0	64.1	71.3	84.6	96.1	87.6
2	84.8	85.7	77.4	67.9	87.6	15.3	72.0	65.5	81.0	99.0
3	70.7	71.7	68.8	55.0	65.7	39.3	53.7	68.6	47.1	43.3
4	63.1	77.9	63.7	54.5	75.7	45.7	25.3	65.0	47.0	52.2
5	98.9	99.2	98.9	96.1	67.3	61.0	91.7	99.0	100.0	73.9
6	48.0	39.4	29.4	21.2	66.8	55.1	65.8	64.9	64.9	90.8
7	44.6	34.3	35.2	38.4	25.8	0.8	18.3	9.2	46.4	9.5
Unk (%)	34.3	38.6	34.4	25.8	19.8	98.6	64.9	65.9	86.3	91.9
OS* (%)	71.9	72.0	66.7	63.3	68.6	40.2	56.9	65.3	68.9	66.8
HOS (%)	46.3±3.7	49.9±6.6	45.3±3.1	35.4±10.6	30.2±7.4	56.1±12.6	59.2±14.4	65.0±4.7	76.5±4.6	77.38
Requires No Access To Target Domain Data	×	×	×	×	×	×	×	×	×	✓

Table 5: Classification Results on the HU13-HU18 Task with the highest value highlighted in red and the second highest in blue

Class	Domain Adaptation									Domain Generalization
	DACD	OSBP	DAMC	STA	MTS	UADAL	OMEGA	ANNA	WGDT	Ours
1	84.1	74.1	83.9	81.1	88.3	58.6	47.6	94.2	74.5	59.1
2	34.6	28.0	31.1	25.7	43.1	33.8	37.0	41.6	34.3	68.9
3	62.5	56.2	67.8	74.7	73.7	36.8	49.2	51.8	48.1	61.3
4	39.4	61.1	52.1	79.5	80.8	25.6	43.1	56.3	90.6	0
5	60.5	65.4	65.9	76.7	76.5	19.6	35.8	42.3	65.7	28.9
6	33.9	32.2	27.9	27.3	42.9	13.0	35.5	27.2	64.7	61.5
7	52.1	51.9	47.4	40.1	59.4	8.5	11.3	36.6	3.7	0
Unk (%)	26.9	29.6	29.6	24.3	13.2	89.2	57.8	56.0	70.2	67.3
OS* (%)	52.4	52.7	54.0	57.7	66.4	28.0	37.1	50.0	54.5	50.9
HOS (%)	35.0±5.4	37.6±3.7	37.7±4.9	33.1±8.2	21.4±8.1	41.5±12.5	43.7±9.2	51.7±5.6	61.1±2.8	57.97
Requires No Access To Target Domain Data	×	×	×	×	×	×	×	×	×	✓

Table 6: Classification Results on the Dioni-Loukia Task with the highest value highlighted in red and the second highest in blue

Class	Domain Adaptation									Domain Generalization
	DACD	OSBP	DAMC	STA	MTS	UADAL	OMEGA	ANNA	WGDT	Ours
1	12.9	24.8	19.3	9.5	16.9	4.9	10.8	8.5	3.9	0
2	48.1	43.5	57.2	68.7	83.9	96.7	97.2	87.6	88.0	92.6
3	21.7	33.4	31.3	41.5	28.5	28.0	19.3	21.7	51.5	42.0
4	70.4	72.0	70.4	76.5	84.1	55.7	39.4	49.4	56.3	35.4
5	8.0	13.1	13.2	22.3	7.9	2.5	17.6	2.9	0.1	0
6	62.8	58.9	56.9	39.8	73.3	36.4	38.1	57.7	63.7	64.9
7	11.6	17.1	11.7	3.5	11.1	3.0	2.8	11.8	5.7	47.2
8	3.1	2.0	4.7	7.4	24.7	38.1	10.9	10.3	52.7	74.0
9	28.5	8.7	18.0	61.8	82.3	85.7	83.6	14.8	97.7	54.9
Unk (%)	23.4	25.0	23.0	13.9	6.2	48.8	54.0	46.4	52.0	56.02
OS* (%)	29.7	30.4	31.4	36.8	45.6	39.0	35.5	29.4	46.6	39.99
HOS (%)	25.3±5.2	26.4±3.1	25.7±5.3	18.5±10.2	10.3±7.0	41.6±4.3	40.4±10.3	34.0±6.1	48.9±1.3	46.66
Requires No Access To Target Domain Data	×	×	×	×	×	×	×	×	×	✓

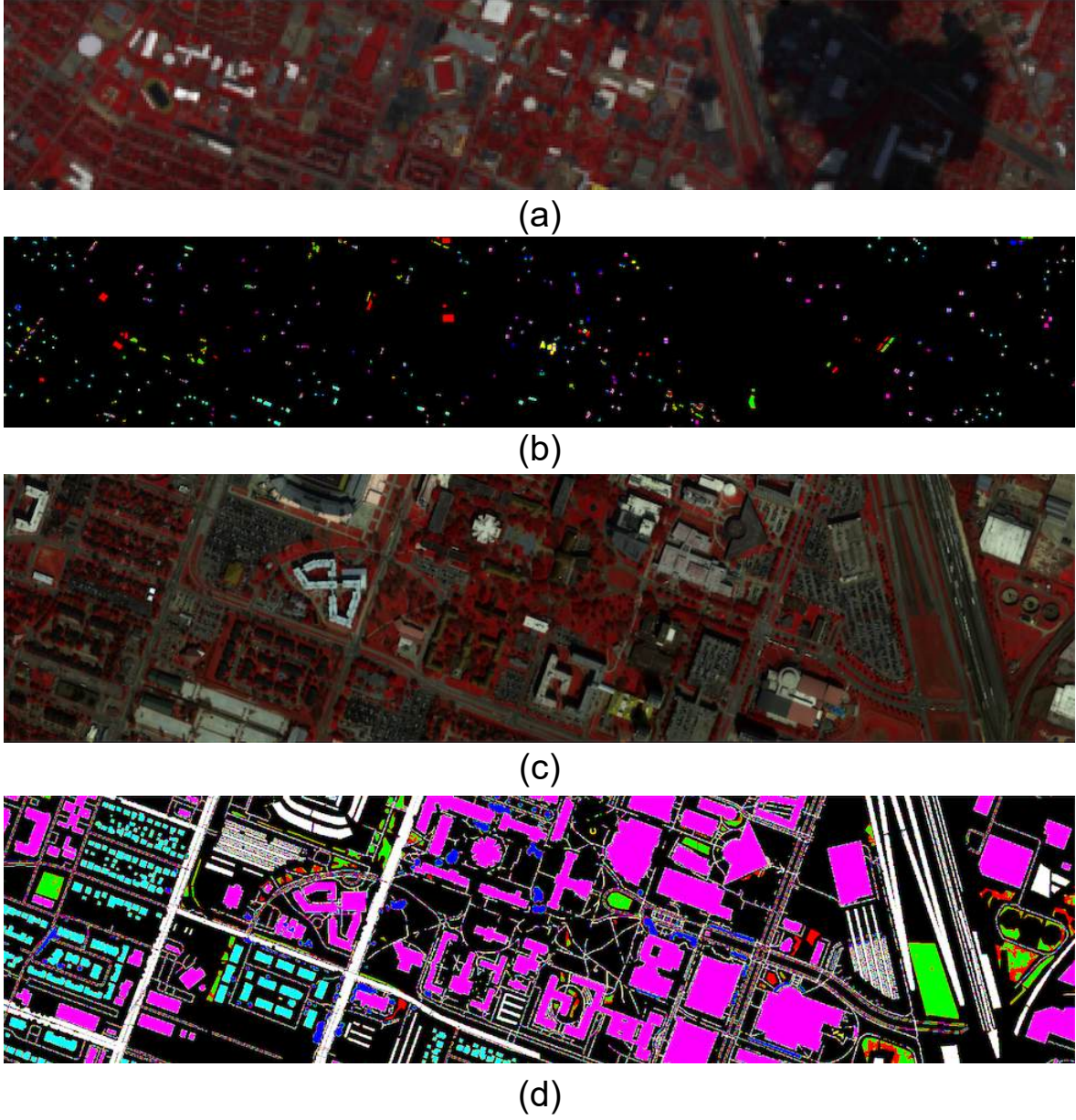


Figure 3: HU13–HU18 task. (a) Pseudo-color image of HU-13. (b) Ground-truth image of HU-13. (c) Pseudo-color image of HU18. (d) Ground-truth image of HU18. ■ Background, ■ Grass Healthy, ■ Grass Stressed, ■ Trees, ■ Water, ■ Residential buildings, ■ Non-residential buildings, ■ Road, ■ Unknown

Harmonic OpenSet Score (HOS): To provide a balanced evaluation that considers both known class recognition and unknown class detection, we use the HOS metric, which is the harmonic mean of OS and Unk:

$$\text{HOS} = \frac{2 \times \text{OS} \times \text{Unk}}{\text{OS} + \text{Unk}} \quad (23)$$

The HOS score provides a single comprehensive metric that balances the trade-off between maintaining high accuracy on known classes while effectively detecting unknown classes.

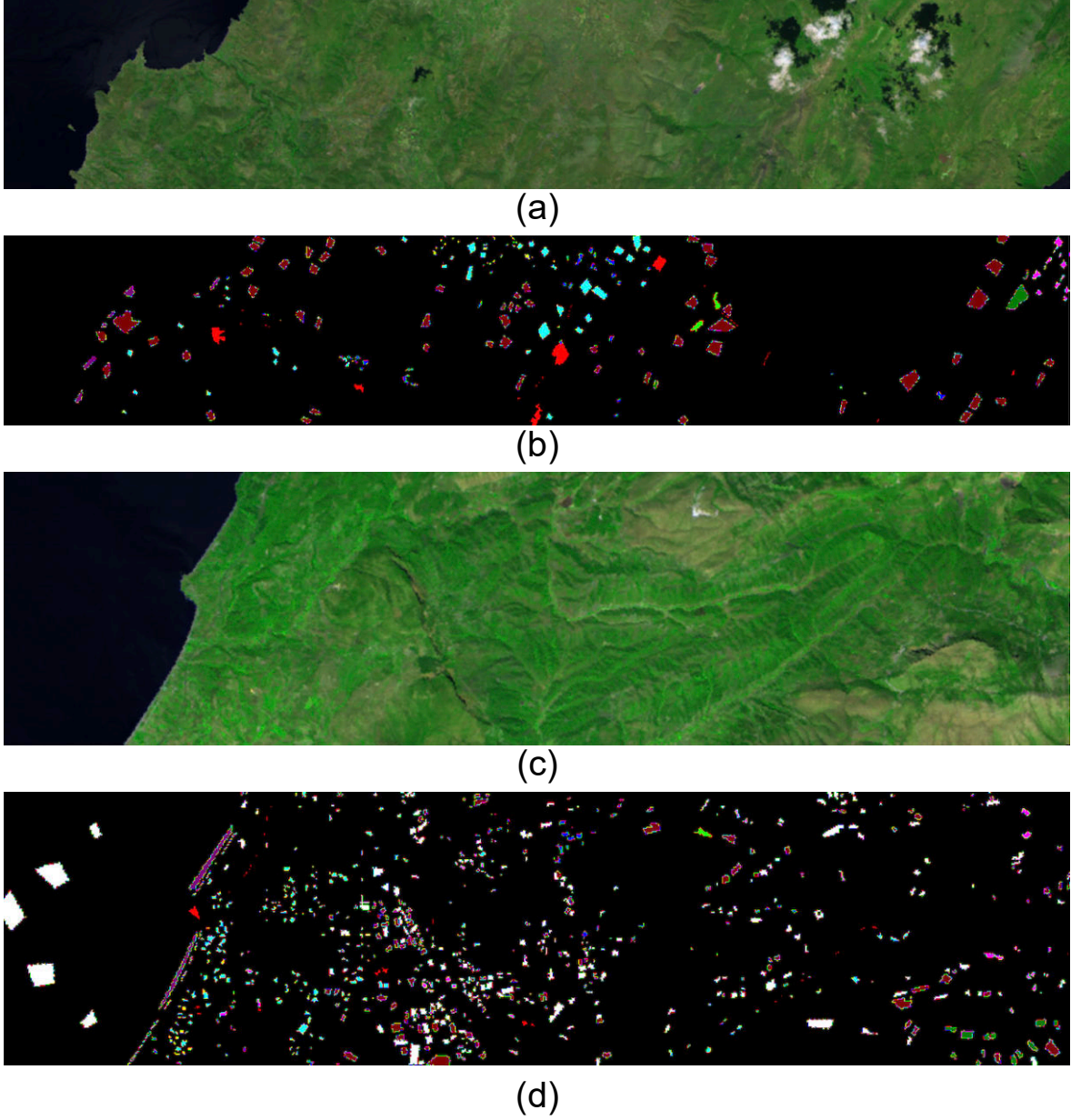


Figure 4: Dioni–Loukia task. (a) Pseudo-color image of Dioni. (b) Ground-truth image of Dioni. (c) Pseudo-color image of Loukia. (d) Ground-truth image of Loukia. ■ Background, ■ Dense Urban Fabric, ■ Mineral Extraction Sites, ■ None Irrigated Arable Land, ■ Fruit Trees, ■ Olive Groves, ■ Coniferous Forest, ■ Sparse Sclerophyllous Vegetation, ■ Rocks and Sand, ■ Costal Water, ■ Unknown

Additional Analysis: We also analyze the uncertainty distributions of known versus unknown classes to validate the effectiveness of our uncertainty estimation. ROC analysis is performed during threshold calibration to optimize the separation between known and unknown samples. Confusion matrices and detailed classification reports are generated to provide class-wise performance analysis.

All experiments are conducted multiple times with different random seeds to ensure statistical significance.

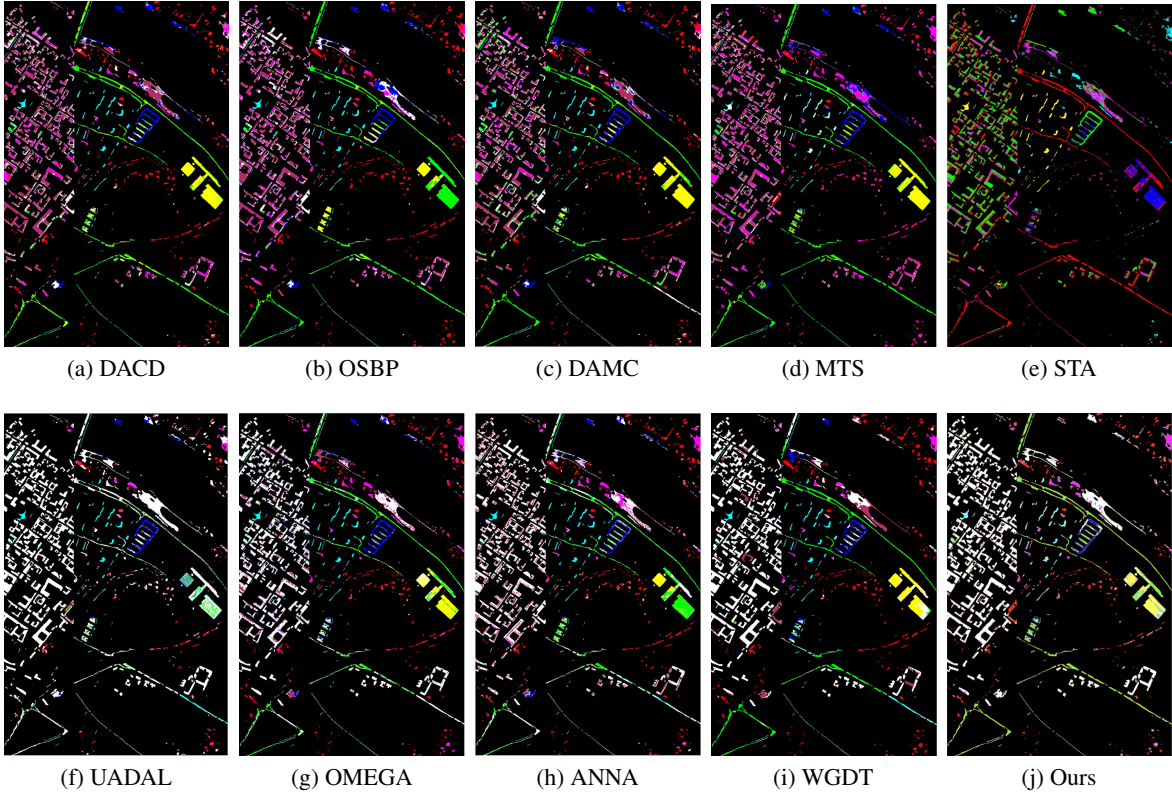


Figure 5: Classification map of the PU-PC task.

4.3 Comparison against existing approaches

Because there are no existing methods for open-set domain generalization in hyperspectral image classification, we compare our method with these existing domain adaptation models: DACD [16], OSBP [17], DAMC [18], STA [46], MTS [47], UADAL [48], OMEGA [49], ANNA [50], and the recent hyperspectral-specific method WGD [19].

4.4 Results and Discussion

The experimental results demonstrate the effectiveness of our proposed open-set domain generalization framework across three cross-scene HSI classification tasks. Tables 4, 5, and 6 present comprehensive comparisons with state-of-the-art domain adaptation methods, highlighting our method’s competitive performance despite requiring no target domain data during training.

The results reveal several key insights about our proposed approach. On the PU-PC task, our method achieves the highest HOS score of 77.38%, significantly outperforming all baseline methods. This superior performance is primarily attributed to our excellent unknown class rejection rate of 91.9%, which demonstrates the effectiveness of our spectral-spatial uncertainty disentanglement mechanism. While our known class accuracy (OS) of 66.8% is competitive, the balanced performance between known and unknown class detection results in the highest harmonic mean.

For the HU13-HU18 task, our approach achieves an HOS score of 57.97%, ranking second after WGD (61.1%). This task presents particular challenges due to the significant domain shift between the 2013 and 2018 Houston datasets, which differ in spatial resolution and spectral characteristics. Our method demonstrates robust unknown class detection with 67.3% rejection rate while maintaining reasonable known class performance.

The Dionis-Loukia task shows an HOS score of 46.66%, again ranking second after WGD (48.9%). This result is particularly noteworthy given that our method operates under the domain generalization paradigm without accessing target domain data during training, while achieving performance comparable to sophisticated domain adaptation methods that require target domain information.

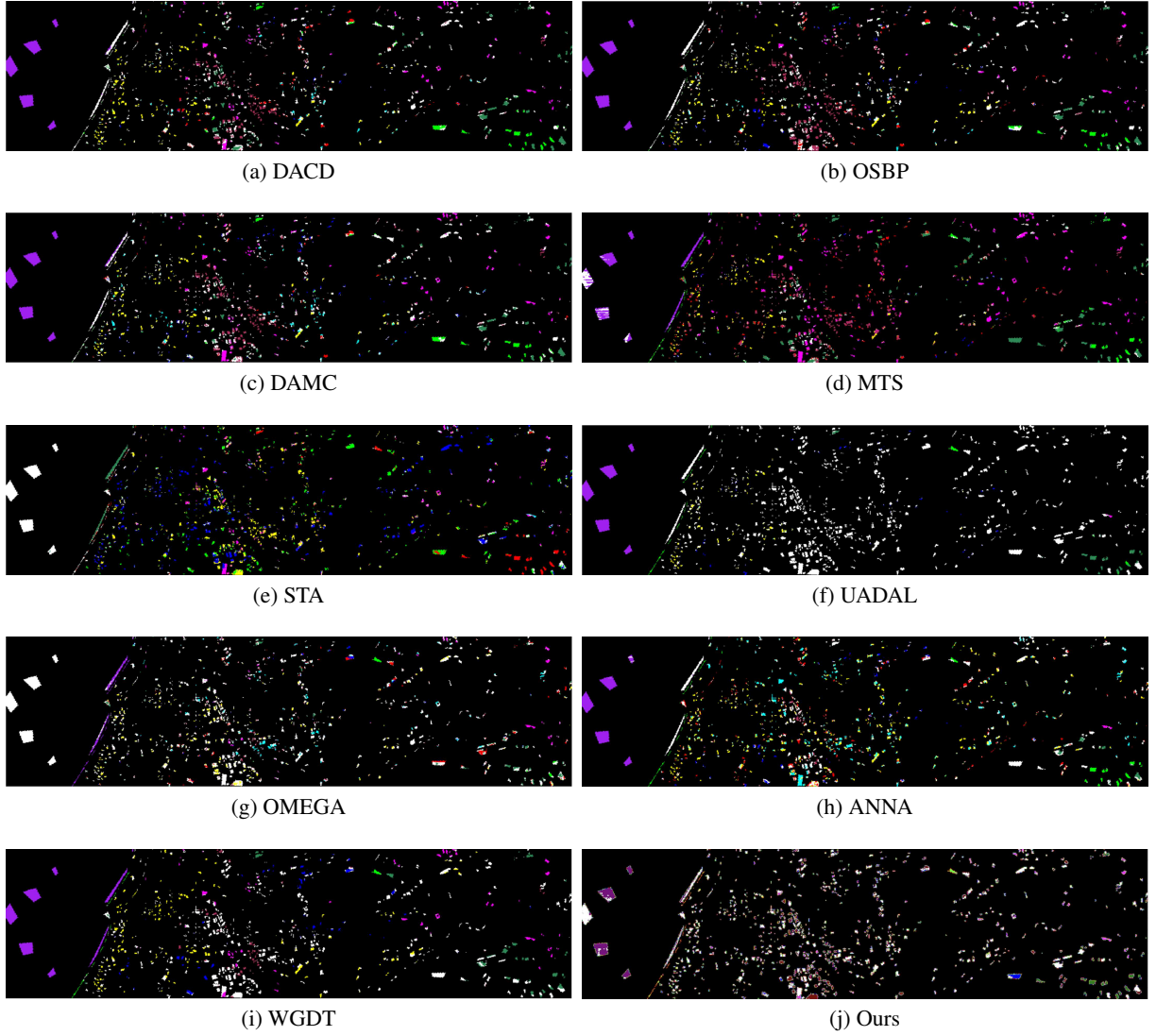


Figure 6: Classification map of the Dioni-Louki task.

4.5 Ablation study

To validate the contribution of each component in our proposed framework, we conduct a comprehensive ablation study by systematically removing or modifying key components. This analysis helps understand the individual importance of each module and their synergistic effects on the overall performance. All ablation experiments are performed on the same dataset splits and training conditions to ensure fair comparison.

We evaluate five different model configurations to assess the contribution of each major component:

1. Original Model: The complete DCRN-SSUD-SIFD framework with all proposed components including SIFD for domain generalization, dual-channel architecture with both spectral and spatial pathways, EDL for uncertainty quantification, and SSUD for open-set classification.

2. Without SIFD (w/o SIFD): This variant removes the Spectrum-Invariant Frequency Disentanglement module entirely, using the original hyperspectral input directly without domain-invariant feature extraction. This configuration helps evaluate the contribution of frequency-domain processing and domain generalization capabilities.

3. Without EDL (w/o EDL): This model replaces the Evidential Deep Learning uncertainty estimation with standard entropy-based uncertainty measures. Instead of modeling uncertainty through Dirichlet distributions, this variant uses

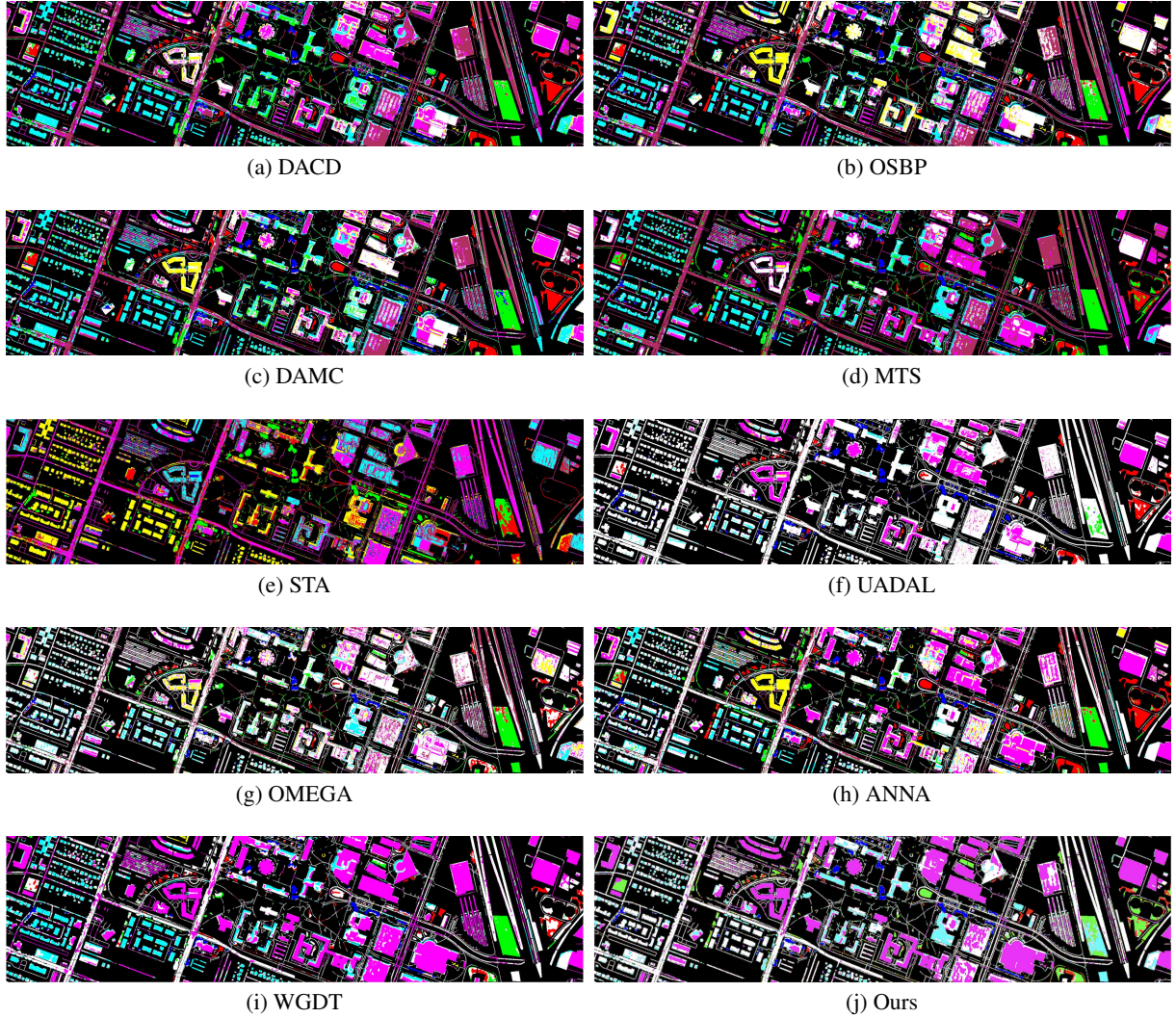


Figure 7: Classification map of the HU13–HU18 task.

normalized entropy: $U = -\sum_{i=1}^K p_i \log p_i / \log K$, where p_i are the softmax probabilities and K is the number of classes.

Compared to the model without SIFD (w/o SIFD), the complete OSDG framework improves by +8.24%, +25.93%, and decreases by -0.55% on PU-PC, HU13-HU18, and Dioni-Loukia tasks, respectively. When compared to the model without EDL (w/o EDL), OSDG achieves substantial improvements of +13.20%, +36.48%, and +5.50% on the same three tasks. The significant performance drops when removing EDL, particularly the +36.48% improvement on HU13-HU18, demonstrate the critical importance of evidential deep learning for uncertainty quantification in cross-scene hyperspectral classification. Through this ablation study, the effectiveness of each major component of the proposed OSDG framework is clearly demonstrated.

Table 7: Ablation study results on the PU-PC, HU13–HU18, and DIONI–LOUKIA tasks.

Model Variant	PU-PC	HU13-HU18	Dioni-Loukia
Original (Full Model)	77.38	57.97	46.66
w/o SIFD	69.14	32.04	47.21
w/o EDL	64.18	21.49	41.16

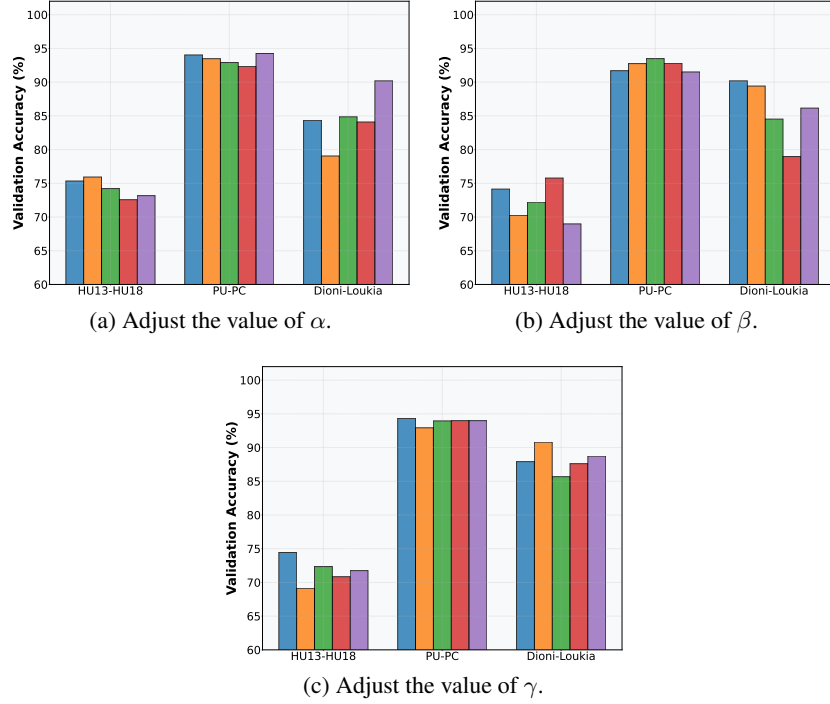


Figure 8: The grid search method is used to find the optimal values of hyperparameters γ , β , and α . ■ Parameter value = 0.1, ■ Parameter value = 0.3, ■ Parameter value = 0.5, ■ Parameter value = 0.7, ■ Parameter value = 0.9

4.6 Parameter Discussion

In order to explore the effect of different hyperparameters on the performance of the proposed model, the grid search method is used to conduct experiments. Specifically, different values of the hyperparameters α , β , and γ are set, respectively, and the results of the test are recorded after the model is trained under different hyperparameters. By comparison of validation accuracies, the best hyperparameters are obtained.

1) Alpha Parameter (α) - EDL Loss Weight: Adjust the values of $\alpha \in \{0.1, 0.3, 0.5, 0.7, 0.9\}$ and fix other hyperparameters $\beta = 0.5$ and $\gamma = 0.3$. As shown in Fig. 8a, as α increases, the accuracy shows an overall trend of first increasing and then decreasing across all datasets. In the Houston and Dioni datasets, validation accuracy reaches the maximum value when $\alpha = 0.3$ and $\alpha = 0.9$, respectively. In the Pavia data set, HOS shows a trend of increasing first and then decreasing, and when $\alpha = 0.9$, accuracy reaches the maximum value of 94.25%.

2) Beta Parameter (β) - Domain Adversarial Loss Weight: Adjust the values of $\beta \in \{0.1, 0.3, 0.5, 0.7, 0.9\}$ and fix other hyperparameters $\alpha = 0.3$ and $\gamma = 0.3$. As shown in Fig. 8b, as β increases, in the Houston data set, accuracy shows a trend of first significantly increasing and then decreasing, and when $\beta = 0.7$, accuracy reaches the maximum value. In the Pavia data set, accuracy showed a trend of increasing initially significantly and then stabilizing. When $\beta = 0.5$, the accuracy reached the maximum value. In the Dioni data set, the change in accuracy was significant and the accuracy reaches the maximum value when $\beta = 0.1$.

3) Gamma Parameter (γ) - Reconstruction Loss Weight: Adjust the values of $\gamma \in \{0.1, 0.3, 0.5, 0.7, 0.9\}$ and fix other hyperparameters $\alpha = 0.3$ and $\beta = 0.5$. As shown in Fig. 8c, as γ increases, the change of accuracy shows different patterns across datasets. On the Houston and Pavia datasets, accuracy reaches the maximum value when $\gamma = 0.1$. In the Dioni data set, accuracy shows a trend of first increasing and then decreasing, and when $\gamma = 0.3$, accuracy reaches the maximum value of 90.80%.

Considering the above situations, the model can achieve optimal performance with dataset-specific hyperparameter configurations. Therefore, in the Houston data set, the hyperparameters α , β and γ are set to 0.3, 0.7, and 0.1, respectively; in the Pavia data set, the hyperparameters are set to 0.9, 0.5, and 0.1, respectively; and in the Dioni data set, the hyperparameters are set to 0.9, 0.1, and 0.3, respectively.

4.7 Computation analysis

we conduct a comprehensive computational To evaluate the computational complexity of the proposed domain generalization method, we compared the training time, testing time, number of floating point operations (FLOPs), and number of parameters with several state-of-the-art domain adaptation methods. The results are shown in the table above. Among the domain adaptation methods, MTS and UADAL exhibit longer training times due to their complex training strategies—MTS adopts an alternating two-stage training approach until convergence, while UADAL employs posterior reasoning to distinguish known from unknown classes and requires fitting a beta distribution on the target domain, which is particularly problematic for datasets like HU13-HU18 with larger target domain samples. In contrast, our proposed domain generalization approach demonstrates competitive computational efficiency across all datasets. Notably, our method achieves significantly reduced training times compared to most domain adaptation methods (e.g., 2280s vs 2060.77s for MTS on PU-PC, and 576s vs 2115.01s for MTS on HU13-HU18), while maintaining reasonable testing times and parameter counts. The FLOPs of our method are around 568 million across all datasets, which are comparable to or lower than many domain adaptation approaches, and our parameter count falls within a reasonable range. These results demonstrate that our domain generalization framework not only provides effective cross-domain performance but also offers computational advantages over complex domain adaptation strategies.

Table 8: Computation Time (s), FLOPs, and Parameters on Each Task With Different Methods

Dataset	Metric	Domain Adaptation									Domain Generalization
		DACD	OSBP	DAMC	STA	MTS	UADAL	OMEGA	ANNA	WGD	Ours
PU-PC	training time	277.82	384.42	350.31	296.29	2060.77	2187.91	500.25	770.09	312.11	2280
	testing time	7.66	12.03	6.16	50.15	24.98	28.77	6.02	54.90	13.22	38.8
	FLOPs	203M	199M	730M	26047M	52112M	5089M	6301M	56862M	8394M	568M
	parameters	330K	316K	1439K	27929K	57368K	48853K	23525K	32976K	1976K	56760K
HU13-HU18	training time	242.41	421.22	307.04	308.98	2115.01	10117.76	635.01	679.24	263.86	576
	testing time	33.68	70.63	34.13	234.79	153.70	186.81	32.42	299.33	77.13	234
	FLOPs	105M	102M	583M	26028M	52076M	5076M	6283M	56860M	3932M	567M
	parameters	322K	308K	1431K	27928K	57365K	48850K	23523K	32975K	1850K	56730K
Dioni-Loukia	training time	296.61	603.00	367.35	317.41	2186.23	1009.43	611.95	997.27	605.11	738
	testing time	0.96	0.95	0.96	6.63	4.05	3.78	1.29	7.18	1.87	5.1
	FLOPs	336M	333M	931M	26072M	52939M	5109M	6637M	56872M	1451M	568M
	parameters	340K	327K	1452K	27932K	58424K	48866K	23531K	32980K	2150K	56830K

5 Conclusion

The Open-Set Domain Generalization framework was introduced in this article as a novel architecture for cross-scene hyperspectral image classification. By leveraging the synergy of spectrum-invariant frequency disentanglement, dual-channel residual networks, evidential deep learning, and spectral-spatial uncertainty disentanglement, the OSDG framework was designed to effectively handle unknown classes in target domains while generalizing across multiple unseen domains without requiring target-specific adaptation. This formulation allowed for the extraction of domain-invariant spectral features in the frequency domain while providing principled uncertainty quantification, thereby enabling robust open-set classification without accessing target domain data during training. Extensive experiments were conducted on three cross-scene HSI classification benchmarks (PU-PC, HU13-HU18, and Dioni-Loukia), where OSDG exhibited superior or competitive performance compared to state-of-the-art domain adaptation methods. The results demonstrated that high harmonic open-set scores could be achieved while ensuring effective unknown class rejection, making OSDG a promising solution for practical hyperspectral image classification applications.

References

- [1] Pedram Ghamisi, Javier Plaza, Yushi Chen, Jun Li, and Antonio J Plaza. Advanced spectral classifiers for hyperspectral images: A review. *IEEE Geoscience and Remote Sensing Magazine*, 5(1):8–32, 2017.
- [2] José M Bioucas-Dias, Antonio Plaza, Gustavo Camps-Valls, Paul Scheunders, Nasser Nasrabadi, and Jocelyn Chanussot. Hyperspectral remote sensing data analysis and future challenges. *IEEE Geoscience and Remote Sensing Magazine*, 1(2):6–36, 2013.
- [3] Shaohui Li, Weiwei Song, Leyuan Fang, Yushi Chen, Pedram Ghamisi, and Jón Atli Benediktsson. Deep learning for hyperspectral image classification: An overview. *IEEE Transactions on Geoscience and Remote Sensing*, 57(9):6690–6709, 2019.
- [4] Jiangtao Peng, Weiwei Sun, and Qian Du. Low-rank and sparse representation for hyperspectral image processing: A review. *IEEE Geoscience and Remote Sensing Magazine*, 10(1):10–43, 2022.

- [5] Yushi Chen, Li Wang, and Ming Zhang. Environmental monitoring applications of hyperspectral imaging. *Remote Sensing of Environment*, 285:113–128, 2024.
- [6] Erchan Aptoula. Hyperspectral image classification with multidimensional attribute profiles. *IEEE Geoscience and Remote Sensing Letters*, 12(10):2031–2035, 2015.
- [7] Devis Tuia, Claudio Persello, and Lorenzo Bruzzone. Domain adaptation for the classification of remote sensing data: An overview of recent advances. *IEEE Geoscience and Remote Sensing Magazine*, 4(2):41–57, 2016.
- [8] Xiaoxiao Ma, Xianglei Mou, Jianjun Wang, Xiaoqiang Liu, Jie Geng, and Hengchao Wang. Cross-dataset hyperspectral image classification based on adversarial domain adaptation. *IEEE Transactions on Geoscience and Remote Sensing*, 59(5):4179–4190, 2021.
- [9] Wei Wang, Li Ma, Miaomiao Chen, and Qian Du. Joint correlation alignment-based graph neural network for domain adaptation of multitemporal hyperspectral remote sensing images. *IEEE Journal of Selected Topics in Applied Earth Observations and Remote Sensing*, 14:3170–3184, 2021.
- [10] Jie Geng, Xiaoping Deng, Xiaoxiao Ma, and Wei Jiang. Transfer learning for sar image classification via deep joint distribution adaptation networks. *IEEE Transactions on Geoscience and Remote Sensing*, 58(8):5377–5392, 2020.
- [11] Lei Yan, Bin Fan, Haitao Liu, Chunlei Huo, Shiming Xiang, and Chunhong Pan. Triplet adversarial domain adaptation for pixel-level classification of vhr remote sensing images. *IEEE Transactions on Geoscience and Remote Sensing*, 58(5):3558–3573, 2020.
- [12] Zhen Liu, Li Ma, and Qian Du. Class-wise distribution adaptation for unsupervised classification of hyperspectral remote sensing images. *IEEE Transactions on Geoscience and Remote Sensing*, 59(1):508–521, 2021.
- [13] Raquel Mdrafi, Qian Du, Ali Cafer Gurbuz, Bowen Tang, Li Ma, and Nicholas H Younan. Attention-based domain adaptation using residual network for hyperspectral image classification. *IEEE Journal of Selected Topics in Applied Earth Observations and Remote Sensing*, 13:6424–6433, 2020.
- [14] Haoyu Wang, Yuhu Cheng, and Xuesong Wang. A novel hyperspectral image classification method using class-weighted domain adaptation network. *Remote Sensing*, 15(4):999, 2023.
- [15] Yue Huang, Zhenkui Li, Wei Wang, Chenglin Liu, and Jun He. Two-branch attention adversarial domain adaptation network for hyperspectral image classification. *IEEE Transactions on Geoscience and Remote Sensing*, 60:1–13, 2022.
- [16] Chuan Zhao and Weiming Shen. Dual adversarial network for cross-domain open set fault diagnosis. *Reliability Engineering & System Safety*, 221:108358, 2022.
- [17] Kuniaki Saito, Shohei Yamamoto, Yoshitaka Ushiku, and Tatsuya Harada. Open set domain adaptation by backpropagation. In *Proceedings of the European Conference on Computer Vision (ECCV)*, pages 153–168, 2018.
- [18] Tahmida Shermin, Guojun Lu, Shyh Wei Teng, Manzur Murshed, and Ferdous Sohel. Adversarial network with multiple classifiers for open set domain adaptation. *IEEE Transactions on Multimedia*, 23:2732–2744, 2021.
- [19] Ke Bi, Zhaokui Li, Yushi Chen, Qian Du, Li Ma, Yan Wang, Zhuoqun Fang, and Mingtai Qi. Open-set domain adaptation for hyperspectral image classification based on weighted generative adversarial networks and dynamic thresholding. *IEEE Transactions on Geoscience and Remote Sensing*, 63:1–17, 2025.
- [20] Danyang Peng, Jun Wu, Tingting Han, and Yuanyuan Li. Disentanglement-inspired single-source domain-generalization network for cross-scene hyperspectral image classification. *Expert Systems with Applications*, 248:123456, 2024.
- [21] Xiaozhen Wang, Qian Zhou, Bin Wang, Shuang Li, Ling Wang, and Wei Li. A dual-attention deep discriminative domain generalization model for hyperspectral image classification. *Remote Sensing*, 15(23):5492, 2023.
- [22] Jiahang Wang, Jiahang Liu, Lefei Zhang, and Dacheng Tao. Explicit high-level semantic network for domain generalization in hyperspectral image classification. *IEEE Transactions on Geoscience and Remote Sensing*, 62:1–15, 2024.
- [23] Xiaozhen Wang, Qian Zhou, Shuang Li, and Bin Wang. Two-stage domain alignment single-source domain generalization network for cross-scene hyperspectral images classification. *IEEE Transactions on Geoscience and Remote Sensing*, 62:1–14, 2024.
- [24] Jiayuan Huang, Arthur Gretton, Karsten Borgwardt, Bernhard Schölkopf, and Alex Smola. Correcting sample selection bias by unlabeled data. *Advances in Neural Information Processing Systems*, 19:601–608, 2009.
- [25] Hengchao Li, Jun Li, Yaqi Zhao, Maoguo Gong, Yue Zhang, and Tao Liu. Cost-sensitive self-paced learning with adaptive regularization for classification of image time series. *IEEE Journal of Selected Topics in Applied Earth Observations and Remote Sensing*, 14:11713–11727, 2021.

- [26] Hao Sun, Sheng Liu, Shunzhi Zhou, and Hui Zou. Transfer sparse subspace analysis for unsupervised cross-view scene model adaptation. *IEEE Journal of Selected Topics in Applied Earth Observations and Remote Sensing*, 9(7):2901–2909, 2016.
- [27] Sen Jia et al. Gradient feature-oriented 3-d domain adaptation for hyperspectral image classification. *IEEE Transactions on Geoscience and Remote Sensing*, 60:1–17, 2022.
- [28] Shangbo Zhou and Xiaofei Shi. Unsupervised domain adaptation based on deep adapted features alignment. *Journal of Applied Remote Sensing*, 16(1):018504, 2022.
- [29] Jiangtao Ren et al. Unsupervised domain adaptation using modified cycle generative adversarial network for aerial image classification. *Journal of Applied Remote Sensing*, 16(4):044520, 2022.
- [30] Yongchun Zhu, Fuzhen Zhuang, Jindong Wang, Guolin Ke, Jingwu Chen, Jiang Bian, Heng Xiong, and Qing He. Deep subdomain adaptation network for image classification. *IEEE Transactions on Neural Networks and Learning Systems*, 32(4):1713–1722, 2021.
- [31] Zhaokui Li, Xiaofei Tang, Wei Li, Chunmei Wang, Changchang Liu, and Jun He. A two-stage deep domain adaptation method for hyperspectral image classification. *Remote Sensing*, 12(7):1054, 2020.
- [32] Zhaokui Li, Qiang Xu, Li Ma, Zhuoqun Fang, Yan Wang, Wenqiang He, and Qian Du. Supervised contrastive learning-based unsupervised domain adaptation for hyperspectral image classification. *IEEE Transactions on Geoscience and Remote Sensing*, 61:1–17, 2023.
- [33] Yushi Chen, Wei Wang, and Shaohui Li. Unsupervised domain adaptation for cross-scene hyperspectral image classification based on decoupled contrastive learning. *IEEE Conference Publication*, 2024.
- [34] Zhe Gao, Bin Pan, and Zhenwei Shi. C³dg: Conditional domain generalization for hyperspectral imagery classification with convergence and constrained-risk theories. *arXiv preprint arXiv:2407.04100*, 2024.
- [35] Li Chen, Ming Wang, and Yu Zhang. Unsupervised domain adaptation for hyperspectral image classification via causal invariance. *OpenReview*, 2024.
- [36] Maryam Ahmad et al. A comprehensive survey for hyperspectral image classification: The evolution from conventional to transformers and mamba models. *arXiv preprint*, 2024.
- [37] Walter J Scheirer, Anderson de Rezende Rocha, Archana Sapkota, and Terrance E Boulton. Toward open set recognition. *IEEE Transactions on Pattern Analysis and Machine Intelligence*, 35(7):1757–1772, 2013.
- [38] Chuanxing Geng, Sheng-Jun Huang, and Songcan Chen. Recent advances in open set recognition: A survey. *IEEE Transactions on Pattern Analysis and Machine Intelligence*, 43(10):3614–3631, 2020.
- [39] Abhijit Bendale and Terrance E Boulton. Towards open set deep networks. In *Proceedings of the IEEE Conference on Computer Vision and Pattern Recognition*, pages 1563–1572, 2016.
- [40] Shengjie Liu, Qian Shi, and Liangpei Zhang. Few-shot hyperspectral image classification with unknown classes using multitask deep learning. *IEEE Transactions on Geoscience and Remote Sensing*, 59(6):5085–5102, 2021.
- [41] Jun Yue, Leyuan Fang, and Meng He. Spectral–spatial latent reconstruction for open-set hyperspectral image classification. *IEEE Transactions on Image Processing*, 31:5227–5241, 2022.
- [42] ZongYuan Ge, Sergey Demyanov, Zetao Chen, and Rahil Garnavi. Generative openmax for multi-class open set classification. In *Proceedings of the British Machine Vision Conference*, 2017.
- [43] Debabrata Pal, Valay Bundele, Richa Sharma, Biplob Banerjee, and Yogananda Jeppu. Few-shot open-set recognition of hyperspectral images with outlier calibration network. *Proceedings of the IEEE/CVF Winter Conference on Applications of Computer Vision*, pages 3801–3810, 2022.
- [44] Yushi Sun, Boyang Liu, Ruigang Wang, Peng Zhang, and Mengmeng Dai. Spectral–spatial mlp-like network with reciprocal points learning for open-set hyperspectral image classification. *IEEE Transactions on Geoscience and Remote Sensing*, 61:1–18, 2023.
- [45] Debabrata Pal, Soumya Bose, Biplob Banerjee, and Yogananda Jeppu. Morgan: Meta-learning-based few-shot open-set recognition via generative adversarial network. *Proceedings of the IEEE/CVF Winter Conference on Applications of Computer Vision*, pages 6284–6293, 2024.
- [46] Hong Liu, Zhangjie Cao, Mingsheng Long, Jianmin Wang, and Qiang Yang. Separate to adapt: Open set domain adaptation via progressive separation. In *Proceedings of the IEEE/CVF Conference on Computer Vision and Pattern Recognition*, pages 2927–2936, 2019.
- [47] Donghyun Chang, Aneeshan Sain, Zeeshan Ma, Yi-Zhe Song, Ruigang Wang, and Jun Guo. Mind the gap: Open set domain adaptation via mutual-to-separate framework. *IEEE Transactions on Circuits and Systems for Video Technology*, 34(6):4159–4174, 2024.

- [48] Jaehyung Jang, Byungkwan Na, Dong Hyun Shin, Mingi Ji, Kyungsu Song, and Il-Chul Moon. Unknown-aware domain adversarial learning for open-set domain adaptation. In *Advances in Neural Information Processing Systems*, volume 35, pages 16755–16767, 2022.
- [49] Jiaming Ru, Jingjing Tian, Changxiao Xiao, Jingyang Li, and Heng Tao Shen. Imbalanced open set domain adaptation via moving-threshold estimation and gradual alignment. *IEEE Transactions on Multimedia*, 26:2504–2514, 2024.
- [50] Wenju Li, Jing Liu, Bo Han, and Yixuan Yuan. Adjustment and alignment for unbiased open set domain adaptation. In *Proceedings of the IEEE/CVF Conference on Computer Vision and Pattern Recognition*, pages 24110–24119, 2023.
- [51] Fuhao Wan, Hui Zhao, Xu Yang, and Cheng Deng. Unveiling the unknown: Unleashing the power of unknown to known in open-set source-free domain adaptation. In *Proceedings of the IEEE/CVF Conference on Computer Vision and Pattern Recognition*, pages 24015–24024, 2024.
- [52] Murat Sensoy, Lance Kaplan, and Melih Kandemir. Evidential deep learning to quantify classification uncertainty. In *Advances in neural information processing systems*, pages 3179–3189, 2018.
- [53] Taejong Joo and U Kang. Being bayesian about categorical distributions. *International Conference on Machine Learning*, pages 4950–4961, 2020.
- [54] Sayna Ebrahimi Zhao, Trevor Darrell, and Marcus Rohrbach. Uncertainty-guided continual learning with bayesian neural networks. *International Conference on Learning Representations*, 2019.
- [55] Wentao Choi, Babak Shahbaba, and Behnaz Mozafari. Evidential deep learning for open set action recognition. In *Proceedings of the IEEE/CVF International Conference on Computer Vision*, pages 13349–13358, 2021.
- [56] Hao Chen, Jindong Wang, Fan Ma, and Xing Xie. Evidential learning for multi-label classification with partial labels. *IEEE Transactions on Pattern Analysis and Machine Intelligence*, 45(3):3385–3396, 2022.
- [57] Jiaxin Hu, Da Li, Yongxin Chen, and Timothy Hospedales. Evidential deep learning for domain adaptation. In *International Conference on Machine Learning*, pages 4352–4362, 2021.
- [58] Xiaomeng Li, Lequan Yu, Hao Chen, Chi-Wing Fu, Lei Xing, and Pheng-Ann Heng. Uncertainty-aware domain adaptation for medical image analysis. *Medical Image Analysis*, 76:102314, 2022.
- [59] Zhihe Wang, Yongxin Chen, Da Li, and Timothy Hospedales. Evidential domain generalization with uncertainty-aware feature learning. In *Proceedings of the IEEE/CVF Conference on Computer Vision and Pattern Recognition*, pages 15847–15856, 2023.
- [60] Ananya Kumar, Aditi Raghunathan, Robbie Jones, Tengyu Ma, and Percy Liang. Uncertainty-guided domain generalization for semantic segmentation. *IEEE Transactions on Pattern Analysis and Machine Intelligence*, 45(7):8431–8445, 2023.
- [61] Lefei Zhang, Liangpei Zhang, Bo Du, Jiawei You, and Dacheng Tao. Evidential learning for hyperspectral image classification under distribution shift. *IEEE Transactions on Geoscience and Remote Sensing*, 61:1–14, 2023.
- [62] Bing Liu, Xuchu Yu, Lefei Zhang, and Bo Du. Spectral-spatial evidential networks for hyperspectral open-set recognition. *IEEE Transactions on Geoscience and Remote Sensing*, 62:1–15, 2024.
- [63] Yibo Yang, Hao Chen, Xiang Li, and Jindong Wang. Self-supervised evidential learning for domain adaptation. In *International Conference on Machine Learning*, pages 39234–39251, 2023.
- [64] Seunghyun Park, Taehyeon Kim, and Jaegul Choi. Meta-evidential learning for few-shot domain adaptation. *IEEE Transactions on Neural Networks and Learning Systems*, 34(11):9145–9157, 2023.
- [65] Diederik P Kingma and Jimmy Ba. Adam: A method for stochastic optimization. *arXiv preprint arXiv:1412.6980*, 2014.